

# Passively-Safe and Robust Multi-Agent Optimal Control with Application to Distributed Space Systems

Tommaso Guffanti<sup>\*</sup> and Simone D'Amico<sup>†</sup>  
*Stanford University, Stanford, California 94305*

This paper develops a novel dynamics, guidance, and control framework that enables a multi-agent system to enforce optimally and efficiently motion safety guarantees even in case of sudden loss of control capabilities by any agent, i.e., guarantees of passive safety (PS). The main application are distributed space systems (DSS) employing miniaturized low-size-weight-and-power and commercial-off-the-shelf technology, which reduce mission financial costs at the expense of reliability. The framework explores the method of variation of parameters, which models the effects of non-integrable dynamics on the integration constants of an integrable portion of the governing dynamics itself, to reduce the number of constraints required to guarantee PS by one polynomial degree in the number of discrete time samples, while compensating for non-integrable dynamics and uncertainty effects. This enables efficient enforcement of PS within a multi-agent optimal control problem solvable using direct methods, as well as the formulation of novel closed-form solutions of DSS PS in closed eccentric orbits. Experimental results on the upcoming VIRTUAL SUPER OPTICS RECONFIGURABLE SWARM (VISORS) flight mission, as well as complementary challenging formation-flying test cases in eccentric orbits, demonstrate the proposed advantage in terms of achieved safety guarantees, control accuracy and gained fuel and computational efficiency.

## I. Introduction

Distributed space systems (DSS) demand high levels of safety, robustness and fault tolerance. Such risk-adversion is mainly dictated by the consequences a collision in space may have both in terms of debris generation and investment losses. In recent years, the trends of spacecraft bus miniaturization and use of low size-weight and power (low-SWaP) as well as commercial-of-the-shelf (COTS) technologies fostered the distribution of payload and tasks among multiple coordinated agents enabling functionalities that are otherwise not achievable by single monolithic systems. On the other hand, these increased the likelihood of contingencies that directly or indirectly cause permanent or temporary incapability to control a spacecraft [1]. Fault-tolerant strategies become therefore fundamental to mitigate the consequences and keep the risks associated to flying such systems within tolerable levels [2]. From a collision safety perspective, different strategies are possible, some notable are: reactive [3], proactive [4], and passive [5–8]. In general terms, reactive means that spacecraft have to re-compute trajectories on-line to avoid collision after a contingency. Proactive can be intended as a variant of reactive, in which the availability of a controlled escape trajectory/maneuver has to be guaranteed at any time even in presence of a degradation, but not complete loss, of control capabilities. Finally, passive means that the controlled trajectories have been pre-designed to guarantee safe separation even in case of sudden loss of control capabilities, being it temporary or permanent. To fly a real space mission, possibly, all these strategies are needed, and must be implemented within the guidance and control pipeline to guarantee safety in the largest number of contingency scenarios. Nevertheless, relying exclusively on a reactive, or even proactive, approach has limitations, not being robust to contingencies that do not permit trajectory re-planning and/or control on the short term of one or multiple spacecraft. This type of contingencies (e.g., sudden bus safe modes, sudden temporary or permanent failure of critical sub-systems) is increasingly common on miniaturized buses employing low-SWaP and COTS components [1], and therefore demand for a passively-safe approach to fault-tolerant collision avoidance. Looking at the literature, examples of reactive and proactive collision avoidance strategies are relatively recent, as the ones proposed in [3, 4]. Whereas, the first attempts of accounting for passive safety (PS) into multi-agent control date back to the 60's with the co-elliptic rendezvous of the Apollo missions [9], and to the 80's with the colocation of geostationary satellites in shared longitude slots [5]. Subsequently, in the last decades, PS became a fundamental enabler of the first binary formation-flying missions in low Earth orbit (LEO) as GRACE, TANDEM-X, PRISMA and BIROS [10]. Here, the relative orbits were designed such as

<sup>\*</sup>Postdoctoral Scholar, Aeronautics and Astronautics, 496 Lomita Mall.

<sup>†</sup>Associate Professor, Aeronautics and Astronautics, 496 Lomita Mall.

safe separation was always guaranteed in the radial/normal orbital directions, irrespective of failures of controlling and/or estimating the separation in the along-track direction [6]. This work has been more recently generalized in literature to  $N$ -spacecraft swarms in near-circular orbit [11]. The main limitations of this literature are: firstly, with the exception of few cases in the closed-proximity operations literature [4, 7] fault-tolerant motion safety strategies are explored at orbit design level [6, 8, 11] and not as a formal constraint within the optimal control problem (OCP); secondly, PS guarantees are given under assumptions on the orbit type and dynamics, e.g., circularity [4, 7] or near-circularity [6, 11], and linearized two-body dynamics [4, 7], or including just specific perturbations [11]; thirdly, PS is enforced through possibly over-conservative constraints on the relative orbit design, e.g., energy matching conditions, sub-state designs [6, 11]. In general, these limitations cause the current state-of-the-art to fall short in addressing the needs required by future DSS missions, both in terms of applicability, breath and robustness.

This paper explores the mathematical method of variation of parameters (VoP) [12, 13] to conceive and develop a novel framework for optimal passively-safe control of multi-agent dynamics systems. Specifically, VoP models the effects of non-integrable dynamics on the integration constants (IC) of an integrable portion of the governing dynamics itself. In this paper, this is used to model efficiently dynamics-dependent constraints with application to fault-tolerant control (as the mentioned PS), and include them within an OCP solvable through direct methods. While being a general method for the solution of both linear and nonlinear ordinary differential equations (ODE) [12], VoP has firstly been developed to model the orbital dynamics [13], assuming the form of the Gauss variational equations (GVE). GVE model the effect of non-integrable orbital perturbations and control accelerations on the keplerian orbital elements (OE), which are IC of the homogeneous part of the governing orbital ODE. Similarly can be said for the relative orbital dynamics linearized for small spacecraft separations. Here, the IC of the homogeneous part are first-order equivalent to the relative orbital elements (ROE) combination of the OE of two spacecraft or a reference orbit and a spacecraft, in both near-circular [14, 15] and eccentric orbits [16, 17] by tuning appropriately their definition. Using VoP and isolating the effect of non-integrable dynamics on the IC state has various advantages. Firstly, it fosters the formulation of highly efficient analytical closed-form dynamics models [18–21]. Secondly, it permits to directly account/compensate for the effects of non-integrable dynamics in guidance and control strategies [11, 22]. Thirdly, it permits to directly specify the "long-term" behavior of the natural motion of the system, which is directly connected to the value of the IC themselves. This comes very handy when motion properties such as collision avoidance have to be enforced over a specified time horizon even in absence of applied control input. This is evident by looking at the DSS literature, where PS is easily obtained by properly selecting the OE or ROE of two resident space objects, as for: co-elliptic rendezvous [8], colocation [5], formation-flying [6]. In addition, given the applicability of VoP to a wider range of dynamical systems [12], the advantages carried by its use are possibly generalizable.

From an algorithmic perspective, this paper looks at the optimization and robotics literature in four topics of motion planning and control. The first topic is open-loop trajectory optimization under state and control constraints. In particular, this paper uses sequential convex programming (SCP), which is a local direct optimization method that seeks the convergence to a local stationary point of a non-convex problem [23] by successively convexifying the non-convex cost and constraints and solving a series of convexified problems. Various SCP algorithms are presented in literature [24, 25], which are characterized by different degrees of application generality and theoretical convergence guarantees. The second topic is robust motion planning, to achieve probabilistic guarantees of constraints satisfaction in presence of system uncertainties. Usually the literature seeks either probabilistic guarantees of safety for a stochastic model of uncertainty or considers a bounded model of uncertainty [26]. Within this paper, the approach is based on the modeling of the uncertainty as linearized Gaussian [27]. In particular, the Kalman filter equations are used to propagate the associated error covariance matrix through the linearization of the dynamics around the estimated mean, and safety margins are computed by using the relevant diagonal components. As additional note, often in literature [28] the covariance propagation is considered not function of the control input, which enables the disjunction of the covariance propagation from the control input computation. In this paper instead, the effect of control and actuation on the uncertainty propagation is explicitly taken into account. This is useful to model the relation between magnitude/direction of the applied control input and the associated execution uncertainty present on spacecraft thrusters. The third topic is model predictive control (MPC) [29], to retrieve closed-loop performances on-line. In particular, in this paper the open-loop robust motion planner is used within a MPC pipeline to retrieve closed-loop performances on-line in presence of unmodeled or mismodeled effects. The fourth topic is multi-agent control, to deploy algorithms on multi-vehicle systems. In general, the computational complexity of checking separation between any couple of agents within an SCP setting scales quadratically with their number [30], this makes the solutions of the centralized multi-agent collision avoidance problem computationally intense for large number of agents. Possible mitigation strategies are limiting the collision checks to a specified subset of neighboring agents [30], or decoupling the problem in a centralized open-loop

planning and a decentralized closed-loop tracking which has to keep the agents within specified tracking error bounds [26]. In this paper the latter approach is followed. Finally, fault tolerance is a largely addressed topic in automatic control literature, assuming diverse connotations in different application fields [31]. On the other hand, looking at the multi-agent control literature specifically, consensus schemes [32] are often used, and fault-tolerance is not included as a formal constraint within the optimization problem. Therefore, this paper addresses the relevant, and not exhaustively explored, problem of efficiently and explicitly enforcing fault-tolerant motion safety guarantees within a multi-agent OCP solvable through direct methods.

This paper builds over the previous work of the authors [33–36] to provide five main contributions to the state-of-the-art. Firstly, in Section II, it demonstrates how VoP and an IC-based state representation can be used for efficient modeling of dynamics-dependent constraints with application to fault-tolerant control, in presence of nonlinear non-integrable dynamics and realistic system uncertainties from sensing, actuation, and unmodeled system dynamics. Secondly, in Section III, it applies this mathematical framework to multi-agent PS, in particular the number of constraints required to guarantee PS is demonstrated being polynomial (super-linear) in the number of time samples, and using IC reduces this number by one polynomial degree, while compensating for non-integrable dynamics and uncertainty effects. Thirdly, in Section IV, it develops an algorithmic framework for solution of the multi-agent passively-safe OCP, which includes a SCP-based centralized algorithm that enforces guarantees of multi-agent PS, and a decentralized tracking logic that reinforces them within an MPC-like closed-loop pipeline. Fourthly, in Section V, it specializes this mathematical and algorithmic framework to the DSS dynamics, and it derives novel closed-form solutions of PS in eccentric orbits, which can be used both for relative orbit design and within a constrained OCP. Finally, in Section VI, it applies the framework to the Virtual Super Optics Reconfigurable Swarm (VISORS) mission [37], a first-of-a-kind nanosatellite segmented telescope due launch in 2024 for high-resolution imaging of the solar corona, and to complementary challenging formation-flying test cases in eccentric orbits. These test cases show the advantages of the proposed approach in terms of achieved safety guarantees, control accuracy and gained fuel and computational efficiency.

## II. The Integration Constants Approach

### A. Mathematical Preliminaries

Let consider a system characterized by an  $s$ -dimensional operational state  $\chi(t) \in \mathbb{R}^s$ , where  $t \in \mathbb{R}_{\geq 0}$  is the independent variable here identified with time. The ODE that governs the operational state is assumed nonlinear control-affine as

$$\dot{\chi}(t) = \mathbf{f}(\chi(t)) + \mathbf{B}(\chi(t))\mathbf{u}(t) \quad (1)$$

with  $\mathbf{u}(t) \in \mathbb{R}^r$  the  $r$ -dimensional applied control input,  $\mathbf{f} : \mathbb{R}^s \rightarrow \mathbb{R}^s$  the drift vector term, and  $\mathbf{B} : \mathbb{R}^s \rightarrow \mathbb{R}^{s \times r}$  the control input matrix. Both  $\mathbf{f}$  and  $\mathbf{B}$  are assumed continuously differentiable. Moreover, let assume the following

**Assumption II.1.** *The system dynamics in Eq. 1 can be partitioned as*

$$\dot{\chi}(t) = \boldsymbol{\iota}(\chi(t)) + \mathbf{d}(\chi(t)) + \mathbf{B}(\chi(t))\mathbf{u}(t) \quad (2)$$

where, the  $\boldsymbol{\iota} : \mathbb{R}^s \rightarrow \mathbb{R}^s$ , is a reduced part of the governing ODE integrable analytically in closed-form, and  $\mathbf{d} : \mathbb{R}^s \rightarrow \mathbb{R}^s$  contains the part of the governing ODE that makes it non-integrable.

Given Assumption II.1, the integration constants (IC) state,  $\mathbf{c} \in \mathbb{R}^s$ , is defined upon analytical integration of  $\boldsymbol{\iota}$  starting at instant  $t_i$ . The IC state elements are independent linear or nonlinear combination of the operational state components at integration instant,  $\chi(t_i)$  (i.e., the initial conditions), and possibly depend on  $t_i$  itself. They are guaranteed to exist as long as Assumption II.1 holds. The choice of IC may vary greatly from system to system, and may reflect quantities that have a clear physical meaning and do conserve under the integrable portion of the dynamics (e.g., energy, angular momentum, etc.) or just be the initial conditions of the system at integration instant. Given this definition, the operational and IC states are linked by the integrated dynamics map  $\chi(t) = \boldsymbol{\psi}(t, \mathbf{c})$ , where  $\boldsymbol{\psi} : \mathbb{R}^{s+1} \rightarrow \mathbb{R}^s$  is defined in closed-form upon integration, and is assumed to be continuous, differentiable, invertible (with the inverse defined as  $\boldsymbol{\psi}^{-1}(t, \chi(t)) : \mathbb{R}^{s+1} \rightarrow \mathbb{R}^s$ ), and possible ambiguities for multivalued functions can be discriminated. Note that the map  $\boldsymbol{\psi}$  is made independent from the integration instant, being it possibly contained within the IC definition itself. If the integrable dynamics is nonlinear, the map  $\boldsymbol{\psi}$  is generally a nonlinear function of the IC. Therefore, its Jacobian  $\boldsymbol{\Psi}(t, \mathbf{c}) = \partial \boldsymbol{\psi}(t, \mathbf{c}) / \partial \mathbf{c} : \mathbb{R}^{s+1} \rightarrow \mathbb{R}^{s \times s}$  is a function of the IC, too. On the contrary, if the integrable dynamics is linear or linearized (i.e.,  $\boldsymbol{\iota}(\chi(t)) \approx \mathbf{A}(t)\chi(t)$ , with  $\mathbf{A} \in \mathbb{R}^{s \times s}$ ), the map  $\boldsymbol{\psi}$  becomes linear with respect to the IC as

$\psi(t, \mathbf{c}) = \Psi(t)\mathbf{c}$ , where now its Jacobian coincides with the fundamental matrix  $\Psi(t) \in \mathbb{R}^{s \times s}$  solution of the linear ODE and just dependent on time. Note that the non-integrable part may include truncated higher-order terms, if a linearization is performed to isolate a linear integrable part.

Variation of parameters (VoP) [12] is a well known mathematical tool that permits to model the effect of non-integrable dynamics on the IC. In particular, a set of ODE of IC variation is derived to rewrite exactly Eq. 2 as

$$\dot{\mathbf{c}}(t) = \mathbf{d}_c(t, \mathbf{c}(t)) + \mathbf{B}_c(t, \mathbf{c}(t))\mathbf{u}(t) \quad (3)$$

where, the drift vector acting on the IC state is defined as  $\mathbf{d}_c(t, \mathbf{c}(t)) = \Psi^{-1}(t, \mathbf{c}(t))\mathbf{d}(\mathbf{c}(t)) : \mathbb{R}^{s+1} \rightarrow \mathbb{R}^s$ , whereas the IC state control input matrix is defined as  $\mathbf{B}_c(t, \mathbf{c}(t)) = \Psi^{-1}(t, \mathbf{c}(t))\mathbf{B}(\mathbf{c}(t)) : \mathbb{R}^{s+1} \rightarrow \mathbb{R}^{s \times r}$ . Eq. 3 shows how both non-integrable dynamics and control have a direct effect on the IC state. On the other hand, they do not alter the structure of the map  $\psi$ . In particular, the motion trajectory of  $\chi(t)$  governed by Eq. 2 is instantaneously contained and tangent to  $\psi(t, \mathbf{c}(t))$ , such as  $\chi(t) = \psi(t, \mathbf{c}(t))$ , with the evolution in time of  $\mathbf{c}(t)$  governed by Eq. 3. From a topological perspective,  $\psi(t, \mathbf{c}(t))$  describes a submanifold of  $\mathbb{R}^s$  on which  $\chi(t)$  lies instantaneously. This idea is known as the "osculation principle" [13].

## B. Efficient Modeling of Dynamics-Dependent Constraints with Application to Fault-Tolerant Control

In this section, the advantage carried by the IC representation regarding the modeling of dynamics-dependent constraints with application to fault-tolerant control is presented in general terms. Then, in Section III, it is applied specifically to the modeling of multi-agent PS. As presented in the introduction, from a fault-tolerant perspective, there is interest in providing guarantees of constraints satisfaction even in case of a sudden loss of control capability. In particular, let consider the state-dependent scalar constraint  $\mathcal{M}(\chi(t)) \leq 0$ , where  $\mathcal{M} : \mathbb{R}^s \rightarrow \mathbb{R}$  is a generic non-convex scalar function of the state, assumed continuously differentiable. The constraint function is assumed scalar for simplicity and because many higher dimensional constraints are decomposable into separated scalar ones. The objective is to enforce such constraint at each instant in the time interval  $[t_0, t_f]$ , and in addition, at each instant in  $(t_i, t_i + T]$ , where  $T \in \mathbb{R}_{\geq 0}$ , considering possible loss of control capability  $\forall t_i \in [t_0, t_f]$ . Under Assumption II.1, this can be formulated in mathematical terms as

$$\begin{aligned} & \{\mathcal{M}(\chi(t)) \leq 0, \quad \forall t \in [t_0, t_f], \\ & \text{such that: } \dot{\chi}(t) = \mathbf{u}(\chi(t)) + \mathbf{d}(\chi(t)) + \mathbf{B}(\chi(t))\mathbf{u}(t)\} \\ & \text{AND} \\ & \{\mathcal{M}(\chi(t)) \leq 0, \quad \forall t \in (t_i, t_i + T], \quad \forall t_i \in [t_0, t_f], \\ & \text{such that: } \dot{\chi}(t) = \mathbf{u}(\chi(t)) + \mathbf{d}(\chi(t))\} \end{aligned} \quad (4)$$

In a discrete time setting, if the interval  $[t_0, t_f]$  is discretized in  $n$  samples, and the intervals  $(t_i, t_i + T]$  in  $m$  samples, and if contingencies are accounted at each of the  $n$  samples, the total number of constraints to be enforced is  $nm$ . In the following, VoP and the IC representation are used reduce such required number of constraints.

To do so, let assume it exists an instant of worst case occurrence of  $\mathcal{M}$  within  $[t_i, t_i + T]$ . In such a way, the satisfaction of the constraint at this instant is a sufficient condition for the satisfaction of the constraint at any other instant within the interval. Mathematically,

$$\exists t^* \in [t_i, t_i + T] : \{\mathcal{M}(\chi(t^*)) \leq 0\} \implies \{\mathcal{M}(\chi(t)) \leq 0, \quad \forall t \in [t_i, t_i + T]\} \quad (5)$$

The instant of worst case occurrence is defined as

$$t^* = \arg \max_{t \in [t_i, t_i + T]} \mathcal{M}(\chi(t)) \quad (6)$$

Moreover, let preliminarily assume that, the non-integrable part of the dynamics is set to zero after a contingency together with the control. Under this assumption, the dynamics after contingency results fully integrable and, therefore,  $\chi(t) = \psi(t, \mathbf{c}(t_i))$ ,  $\forall t \in [t_i, t_i + T]$ . Note that the IC state is a linear or nonlinear combination of  $\chi(t_i)$  and possibly  $t_i$  itself. Under this assumption, Eq. 6 can be rewritten as

$$t^* = \arg \max_{t \in [t_i, t_i + T]} \mathcal{M}(\psi(t, \mathbf{c}(t_i))) \quad (7)$$

where,  $\mathbf{c}(t_i)$  is a constant, by definition, under integrable dynamics. Note that in Eq. 7,  $\mathcal{M}$  is a closed-form expression of time, which is the optimization variable, whereas the IC state acts as a parameter vector in the optimization. Being  $\mathcal{M}$

a generic non-convex function of the state, and in general, being  $\psi$  a non-convex function of time, Eq. 7 is a non-convex parametric optimization problem, in the parameter vector  $\mathbf{c}(t_i)$ . By definition, the solution of a parametric optimization problem is function of the parameters themselves. Therefore, by definition,  $t^*$  is a function of the IC. This function is assumed here identifiable as  $t^* = t^*(\mathbf{c}(t_i)) : \mathbb{R}^s \rightarrow \mathbb{R}_{\geq 0}$ . Under the assumption of integrability of the dynamics after contingency, this permits to rewrite the sufficient condition in Eq. 5 as

$$\mathcal{M}(\chi(t^*)) = \mathcal{M}\left(\psi(t^*(\mathbf{c}(t_i)), \mathbf{c}(t_i))\right) = \mathcal{M}^*(\mathbf{c}(t_i)) \leq 0 \quad (8)$$

which makes the constraint a function of the IC state evaluated at the contingency instant independent from the time along the uncontrolled trajectory:  $\mathcal{M}^*(\mathbf{c}(t_i)) : \mathbb{R}^s \rightarrow \mathbb{R}$ . Removing the dependency from the time along the uncontrolled trajectories has an important implication

**Remark II.2.** *Assuming integrability of the dynamics after contingency, fault-tolerant constraint satisfaction is achieved for at least  $T$  after contingency, by enforcing as many constraints as the number of possible contingency instants.*

In particular, enforcing Eq. 8 in place of Eq. 4 implies a reduction of the number of constraints by one polynomial degree in the number of discrete time samples, from  $nm$  to  $n$ . In Eq. 8, the formalization of the function  $\mathcal{M}^*$  assumes the capability of identifying the function  $t^*(\mathbf{c}(t_i))$ . In this paper, a general algorithmic procedure is proposed in Section IV, moreover, closed-form solutions applied to DSS PS are presented in Section V. Furthermore, Remark II.2 assumes the integrability of the dynamics after contingency. Nevertheless, VoP can be used to make Eq. 8 robust to non-integrable dynamics effects. This is done by bounding the integrated effect of non-integrable dynamics on  $\mathcal{M}^*$  over  $[t_i, t_i + T]$  as

$$\left| \frac{\partial \mathcal{M}^*(\mathbf{c})}{\partial \mathbf{c}} \right|_{\mathbf{c}(t_i)} \int_{t_i}^{t_i+T} \mathbf{d}_c(\tau, \mathbf{c}(\tau)) d\tau \leq \beta(t_i, T) \quad (9)$$

In Eq. 9,  $\partial \mathcal{M}^*/\partial \mathbf{c} \in \mathbb{R}^s$  is a Jacobian vector mapping the integrated effect of non-integrable dynamics to a net variation of  $\mathcal{M}^*$ , whereas,  $\beta \in \mathbb{R}_{\geq 0}$  is a bounding constant. This constant is added to Eq. 8 as

$$\mathcal{M}^*(\mathbf{c}(t_i)) + \beta(t_i, T) \leq 0 \quad (10)$$

to compensate for non-integrable dynamics effects on constraint satisfaction. In the following, the deterministic analysis developed in this section is generalized to account for bounded effects of uncertainties on the constraint satisfaction.

### C. Inclusion of Uncertainties

Let consider now a closed-loop control setting where the system has to find a control plan  $\tilde{\mathbf{u}}(t) \in \mathbb{R}^r$ , for  $t \in [t_0, t_f]$ , to move from an initial configuration at  $t_0$  to a target one at  $t_f$ , acquiring at instants  $t_e \in [t_0, t_f]$  an updated estimate of its IC state  $\tilde{\mathbf{c}}_e \in \mathbb{R}^s$ . Such estimate is the mean of a Gaussian distribution  $\mathcal{N}(\tilde{\mathbf{c}}_e, \mathbf{C}_e)$ , provided by on-board sensing and navigation, where  $\mathbf{C}_e \in \mathbb{R}^{s \times s}$  is the error covariance matrix. Note that, depending on the the estimation filter implementation, such Gaussian distribution may be provided on the operational state  $\mathcal{N}(\tilde{\mathbf{X}}_e, \mathbf{X}_e)$ , with  $\tilde{\mathbf{X}}_e \in \mathbb{R}^s$  and  $\mathbf{X}_e \in \mathbb{R}^{s \times s}$ , and then mapped to the IC state inverting the integrated dynamics closed-form map as  $\tilde{\mathbf{c}}_e = \psi^{-1}(t_e, \tilde{\mathbf{X}}_e)$  and  $\mathbf{C}_e = \Psi^{-1}(t_e, \tilde{\mathbf{c}}_e) \mathbf{X}_e \Psi^{-T}(t_e, \tilde{\mathbf{c}}_e)$ , where  $(\cdot)^T$  means transpose. Moreover, let assume the system has available on-board a nonlinear dynamics model,  $\tilde{\mathbf{d}}_c : \mathbb{R}^{s+1} \rightarrow \mathbb{R}^s$ , approximating the real effect of non-integrable dynamics on the IC. Using this model and VoP, the system propagates on-board the estimated mean IC state as

$$\dot{\tilde{\mathbf{c}}}(t) = \tilde{\mathbf{d}}_c(t, \tilde{\mathbf{c}}(t)) + \mathbf{B}_c(t, \tilde{\mathbf{c}}(t)) \tilde{\mathbf{u}}(t) \quad (11)$$

Given this available on-board dynamics, let assume the system uses a linearized approach of propagation of uncertainties. The evolution in time of the Gaussian approximation of the uncertainty distribution is modeled through a linear ODE governing the state error covariance matrix [27]. To formalize this ODE, the discrepancy between the real non-integrable dynamics and the available approximation:  $\tilde{\mathbf{d}}_c(t, \tilde{\mathbf{c}}(t)) - \mathbf{d}_c(t, \mathbf{c}(t))$ , is modeled as zero-mean white Gaussian process-noise with power spectral density  $\mathbf{Q}(t) \in \mathbb{R}^{s \times s}$ . The process noise power spectral density and covariance may be time-dependent, but no time correlation is assumed to exist. Furthermore, the discrepancy introduced by the actuation system between the planned control input and the real applied control input:  $\tilde{\mathbf{u}}(t) - \mathbf{u}(t)$ , is modeled as a zero-mean white Gaussian noise with power spectral density  $\mathbf{U}(t) \in \mathbb{R}^{r \times r}$ , also in this case no time correlation is assumed to exist. On the other hand, as anticipated in the introduction, the relation between planned control input and

associated execution uncertainty is modeled, as:  $\mathbf{U}(t) = \mathcal{U}(\tilde{\mathbf{u}}(t)) + \tilde{\mathbf{U}}(t)$  where  $\mathcal{U} : \mathbb{R}^r \rightarrow \mathbb{R}^{r \times r}$  and  $\tilde{\mathbf{U}}(t) \in \mathbb{R}^{r \times r}$  is a remaining aleatory component independent from the planned control. Finally, the effect of future expected measurements on the state error covariance is modeled with an impulsive function:  $\mathbf{E}(t) = \delta(t - t_{\tilde{e}})\mathcal{E}(\mathbf{C}_{\tilde{e}})$  where the Dirac-delta equals to one at the future predicted measurements instants  $t_{\tilde{e}}$ , and  $\mathcal{E} : \mathbb{R}^{s \times s} \rightarrow \mathbb{R}^{s \times s}$  is a function of the predicted future estimated state covariance  $\mathbf{C}_{\tilde{e}}$ . Modeling the effect to future measurements on the covariance is important, since it permits to inform the controller of the expected closed-loop behavior of the covariance even when it has to solve for an open-loop plan. This prevents possible unfeasibility of the open-loop control solution, due to the growth of the uncertainty propagated in open-loop. Given these models, the linear ODE governing the IC state error covariance matrix  $\mathbf{C}(t)$  is [27]

$$\dot{\mathbf{C}}(t) = \tilde{\mathbf{D}}_c(t, \tilde{\mathbf{c}}(t), \tilde{\mathbf{u}}(t))\mathbf{C}(t) + \mathbf{C}(t)\tilde{\mathbf{D}}_c^T(t, \tilde{\mathbf{c}}(t), \tilde{\mathbf{u}}(t)) + \mathbf{B}_c(t, \tilde{\mathbf{c}}(t))\mathbf{U}(t)\mathbf{B}_c^T(t, \tilde{\mathbf{c}}(t)) + \mathbf{Q}(t) + \mathbf{E}(t) \quad (12)$$

where  $\tilde{\mathbf{D}}_c = \partial \tilde{\mathbf{d}}_c / \partial \mathbf{c} \big|_{\tilde{\mathbf{c}}} + \partial \mathbf{B}_c / \partial \mathbf{c} \big|_{\tilde{\mathbf{c}}} \tilde{\mathbf{u}} : \mathbb{R}^{s+r+1} \rightarrow \mathbb{R}^{s \times s}$ . The Jacobians and the control input matrix are evaluated at the mean state estimate, therefore, Eq. 12 holds accurately just in the neighborhood of the mean state estimate itself.

### 1. Robustification of Fault-Tolerant Constraint Formulation

It is of interest to make Eq. 10 applicable in this real closed-loop control setting, robustifying it against the modeled uncertainties evaluated at a specified  $q$ - $\sigma$  confidence level (with  $q \in \mathbb{N}_{>0}$  and  $\sigma$  being a statistical standard deviation). To do so, the integrated effect of non-integrable dynamics and uncertainty on  $\mathcal{M}^*$  over  $[t_i, t_i + T]$  are bounded using VoP as

$$\left| \frac{\partial \mathcal{M}^*(\mathbf{c})}{\partial \mathbf{c}} \bigg|_{\tilde{\mathbf{c}}(t_i)} \int_{t_i}^{t_i+T} \tilde{\mathbf{d}}_c(\tau, \tilde{\mathbf{c}}(\tau)) d\tau \right| + \left| \frac{\partial \mathcal{M}^*(\mathbf{c})}{\partial \mathbf{c}} \bigg|_{\tilde{\mathbf{c}}(t_i)} q \sqrt{\text{Diag} \left( \int_{t_i}^{t_i+T} \left( \tilde{\mathbf{D}}_c(\tau, \tilde{\mathbf{c}}(\tau))\mathbf{C}(\tau) + \mathbf{C}(\tau)\tilde{\mathbf{D}}_c^T(\tau, \tilde{\mathbf{c}}(\tau)) + \mathbf{Q}(\tau) \right) d\tau + \mathbf{C}(t_i) \right)} \right| \leq \beta(t_i, T, q) \quad (13)$$

where  $\partial \mathcal{M}^* / \partial \mathbf{c} \in \mathbb{R}^s$  is a Jacobian vector, the  $\text{Diag}(\cdot)$  operator extracts the diagonal vector from a square matrix, the absolute value  $|\cdot|$  is applied element-wise for vector quantities,  $q \in \mathbb{N}_{>0}$  models the  $q$ - $\sigma$  uncertainty level considered, and  $\tilde{\mathbf{c}}(t_i)$  and  $\mathbf{C}(t_i)$  are obtained by propagating Eq. 11-12 up to contingency instant  $t_i$ . In Eq. 13,  $\beta \in \mathbb{R}_{\geq 0}$  is an enlarged bounding constant with respect to the one defined in Eq. 9, which permits to compensate for both non-integrable dynamics and uncertainty effects on the fault-tolerant constraint satisfaction, as

$$\mathcal{M}^*(\tilde{\mathbf{c}}(t_i)) + \beta(t_i, T, q) \leq 0 \quad (14)$$

where now the function  $\mathcal{M}^*$  is evaluated at the mean IC state estimate.

## D. Efficient Formulation of the Fault-Tolerant Optimal Control Problem

Given this discussion, in closed-loop, the OCP the system must solve, possibly at every instant  $t_e \in [t_0, t_f]$  an updated state estimate is available, until a specified target set  $\mathcal{C}_f$  is reached at  $t_f$ , is

### Problem II.3.

$$\begin{aligned} & \underset{\tilde{\mathbf{u}}(t)}{\text{minimize}} && \int_{t_e}^{t_f} \mathcal{J}(\tilde{\mathbf{c}}(t), \mathbf{C}(t), \tilde{\mathbf{u}}(t), t) dt \\ & \text{subject to} && \dot{\tilde{\mathbf{c}}}(t) = \tilde{\mathbf{d}}_c(t, \tilde{\mathbf{c}}(t)) + \mathbf{B}_c(t, \tilde{\mathbf{c}}(t))\tilde{\mathbf{u}}(t) && \forall t \in [t_e, t_f] \\ & && \dot{\mathbf{C}}(t) = \tilde{\mathbf{D}}_c(t, \tilde{\mathbf{c}}(t), \tilde{\mathbf{u}}(t))\mathbf{C}(t) + \mathbf{C}(t)\tilde{\mathbf{D}}_c^T(t, \tilde{\mathbf{c}}(t), \tilde{\mathbf{u}}(t)) + && \forall t \in [t_e, t_f] \\ & && \quad + \mathbf{B}_c(t, \tilde{\mathbf{c}}(t))\mathbf{U}(t)\mathbf{B}_c^T(t, \tilde{\mathbf{c}}(t)) + \mathbf{Q}(t) + \mathbf{E}(t) && \\ & && \mathcal{M}^*(\tilde{\mathbf{c}}(t)) + \beta(t, T, q) \leq 0 && \forall t \in [t_e, t_f] \\ & && \tilde{\mathbf{u}}(t) \in \mathcal{U} && \forall t \in [t_e, t_f] \\ & && \mathcal{N}(\tilde{\mathbf{c}}(t_f), \mathbf{C}(t_f)) \in \mathcal{C}_f \\ & && \tilde{\mathbf{c}}(t_e) = \tilde{\mathbf{c}}_e \text{ and } \mathbf{C}(t_e) = \mathbf{C}_e \end{aligned} \quad (15)$$

Where,  $\mathcal{J} \in \mathbb{R}_{>0}$  is a generic cost functional modeling control input and/or time minimization as well as other factors,  $\mathcal{U}$  is the set of admissible control inputs, and the bound  $\beta(t_i, T, q)$  is defined as in Eq. 13. The control horizon progressively contracts from  $[t_0, t_f]$  to zero, while  $t_e \rightarrow t_f$ . This represents a generic MPC-like implementation that permits to retrieve closed-loop properties by recomputing the control plan when an updated state estimate is available. Problem II.3 enforces fault-tolerant constraint satisfaction for at least  $T$  after contingency, at  $q$ - $\sigma$  confidence, at the cost of checking as many constraints as the number of possible contingency instants in  $[t_e, t_f]$ . This implies a reduction of the number of constraints by one polynomial degree in the number of discrete time samples with respect to the formulation in Eq. 4 (i.e., from  $nm$  to  $n$ ). Problem II.3 is a non-convex optimization problem, which can be solved, for example, using direct methods, as discussed in Section IV.

### III. Multi-Agent Passively-Safe Optimal Control

In this section, the developed framework is used to efficiently enforce the constraint of multi-agent PS, which is defined in this paper as follows

**Definition III.1. Passive Safety (PS) on  $[t_0, t_f]$ , for at least  $T$ , of at least  $\epsilon$ , at  $q$ - $\sigma$  confidence.** Along the trajectory towards the target condition, a multi-agent system is defined passively-safe if all the agents maintain a separation of at least  $\epsilon$ , accounting for  $q$ - $\sigma$  uncertainties, even in case any agent loses control at any instant  $t \in [t_0, t_f]$  without possibility of re-planning until  $t_f + T$ .

Note that, in principle, it is possible to distinguish between different PS classes depending on the type of failure causing the loss of control capabilities. For example, it is possible to distinguish between hard failures, which prevent re-planning capabilities on the short term, or temporary failures, which allow re-planning capabilities on the short term. Furthermore, in the multi-agent setting, it is possible to account just for the loss of control of a specified subset of agents. PS as defined in Definition III.1, is a rather conservative class, in which any subset or combination of agents may lose control at any instant in  $[t_0, t_f]$ , without being able to recover it and re-plan to avoid collision until  $t_f + T$ . The intention is to set the bar for milder PS classes, which can be deducted by down-grading the one addressed in this paper. Note that Definition III.1 directly accounts for the presence of possible "permanently passive" agents, whose trajectory is uncontrolled since  $t_0$ . The presence of such passive agents is relevant to the DSS application, where a subset of spacecraft may be orbiting passively. Both for active and permanently passive agents, the formulation in this paper relies on the capability to retrieve an estimate of their state through sensing, navigation and prediction. A graphical comparison between this class of PS and the standard collision avoidance is presented in Figure 1. The controlled trajectories of the active agents are in solid lines, the uncontrolled ones in dashed lines, the shaded blue ellipses represent the uncertainty distributions of the Cartesian positions evaluated at  $q$ - $\sigma$  confidence interval.

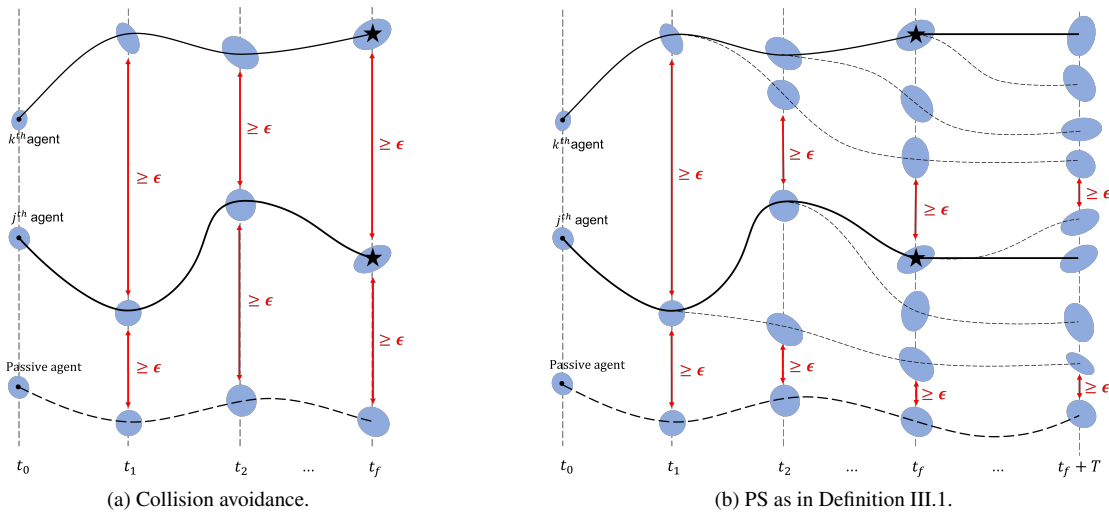


**Fig. 1 Comparison between standard collision avoidance and PS.**

In order to describe PS mathematically, let consider a multi-agent system in the Cartesian space, composed by

$N \in \mathbb{N}_{>0}$  agents, of which  $N_a \in \mathbb{N}_{>0}$  are active and controlled, whereas  $N_p \in \mathbb{N}_{>0}$  are permanently passive from  $t_0$ . By definition,  $N_a + N_p = N$ . The operational state  $\mathcal{X}_k(t)$  of each  $k^{th}$  agent includes at the top the Cartesian position of the agent's center of mass, and is governed by Eq. 1. For the permanently passive agents,  $\mathbf{u}(t) = \mathbf{0}$ ,  $\forall t \geq t_0$ . Whereas, for active agents, control goes to zero just after contingencies possibly happening on  $[t_0, t_f]$ . Let define with  $\mathcal{X}_k(t|t_i)$  the operational state of  $k^{th}$  agent on the uncontrolled trajectory generated at instant  $t_i$ . If  $k^{th}$  agent is active,  $t_i$  is the contingency instant; if it is permanently passive  $t_i = t_0$  by definition. Furthermore, let define as  $\mathcal{S}_{k_j i l}(t) = \|\mathcal{S}(\mathcal{X}_k(t|t_i) - \mathcal{X}_j(t|t_l))\|_2 \in \mathbb{R}_{\geq 0}$  the separation reached at time  $t$  by  $k^{th}$  and  $j^{th}$  agents on the uncontrolled trajectories generated at instants  $t_i$  and  $t_l$  respectively. The matrix  $\mathcal{S} \in \mathbb{N}^{3 \times s}$  selects the components of the Cartesian position within the state, and  $\|\cdot\|_2$  is the  $L_2$ -norm. Reasoning deterministically, PS can be formulated by using Eq. 4, with the  $\mathcal{M}$ -function defined as

$$\mathcal{M}(\mathcal{X}_k(t), \mathcal{X}_j(t)) = \epsilon - \mathcal{S}_{k_j i l}(t) = \epsilon - \|\mathcal{S}(\mathcal{X}_k(t|t_i) - \mathcal{X}_j(t|t_l))\|_2 \quad (16)$$

$\forall t_i \in [t_0, t_f], \forall t_l \in [t_0, t_f], \forall t \in [\max\{t_i, t_l\}, t_f + T], k = 1, \dots, N-1, j = k+1, \dots, N$ . Where, for example, if  $j^{th}$  agent is permanently passive then  $t_l = t_0$ . Using the  $\mathcal{M}$ -formulation defined in Eq. 16, the computational requirements in terms of number of constraints to be enforced are reported in Table 1 on the top, and formal proof is developed in Appendix VIII.A. The interval  $[t_0, t_f]$  is discretized in  $n$  samples, whereas the interval  $(t_f, t_f + T]$  in  $m$  samples. A distinction between "continuous" and "impulsive" control types is made. In particular, in the continuous type, control may be applied and possibly lost at each of the  $n$  sample instants in  $[t_0, t_f]$ . In the impulsive type, control/maneuvers may be applied and possibly failed just in a subset  $n_M \leq n$  of the  $n$  instants, assuming for simplicity that the ratio  $n/n_M \in \mathbb{N}_{>0}$ . In both control types, safe separation must be enforced at each of the  $n$  and  $m$  instants. This guarantees that even the uncontrolled arcs in between impulsive maneuvers are collision free. The number of constraints required to enforce PS between active agents are reported in Table 1 on the left, whereas between active and permanently passive agents on the right. To summarize, using the  $\mathcal{M}$ -formulation, for both control types, the number of constraints to be enforced is cubic in the number of discrete time samples for PS between active agents, whereas quadratic in the number of discrete time samples for PS between active and permanently passive agents. For  $n_M \rightarrow n$ , the number of constraints required in impulsive control tends to the ones required in continuous control, without affecting the polynomial degree behavior. The number of constraints scales quadratically with the number of agents.

**Table 1** Passive Safety constraint requirements. Numerical examples are shown in Figure 2.

Formulation	Control type	Constraints Between Active Agents		Constraints Between Active and Permanently Passive Agents	
		#	$\mathcal{O}(\cdot)$	#	$\mathcal{O}(\cdot)$
$\mathcal{M}$	Continuous	$\left\{ \frac{n(n+1)(2n+1)}{6} + (n+1)^2 m \right\} \frac{N_a(N_a-1)}{2}$	$(n+m)n^2 N_a^2$	$\left\{ \frac{n(n+1)}{2} + (n+1)m \right\} N_a N_p$	$(n+m)n N_a N_p$
	Impulsive	$\left\{ \frac{n}{n_M} \left( \frac{n_M(n_M+1)(2n_M+1)}{6} \right) + (n_M+1)^2 m \right\} \frac{N_a(N_a-1)}{2}$	$(n+m)n_M^2 N_a^2$	$\left\{ \frac{n}{n_M} \left( \frac{n_M(n_M+1)}{2} \right) + (n_M+1)m \right\} N_a N_p$	$(n+m)n_M N_a N_p$
$\mathcal{M}^*$	Continuous	$\frac{n^2 N_a(N_a-1)}{2}$	$n^2 N_a^2$	$n N_a N_p$	$n N_a N_p$
	Impulsive	$\frac{n_M^2 N_a(N_a-1)}{2}$	$n_M^2 N_a^2$	$n_M N_a N_p$	$n_M N_a N_p$

By introducing Assumption II.1, this high number of constraints is reduced. In particular, the procedure presented in Section II is applied and, under the assumption of integrability of the dynamics after contingency, the  $\mathcal{M}^*$ -function is defined as

$$\mathcal{M}^*(\mathbf{c}_k(t_i), \mathbf{c}_j(t_l)) = \epsilon - \mathcal{S}_{k_j i l}^*(\mathbf{c}_k(t_i), \mathbf{c}_j(t_l)) = \epsilon - \left\| \mathcal{S} \left( \boldsymbol{\psi}(t_{k_j i l}^*(\mathbf{c}_k(t_i), \mathbf{c}_j(t_l)), \mathbf{c}_k(t_i)) - \boldsymbol{\psi}(t_{k_j i l}^*(\mathbf{c}_k(t_i), \mathbf{c}_j(t_l)), \mathbf{c}_j(t_l)) \right) \right\|_2 \quad (17)$$

$\forall t_i \in [t_0, t_f], \forall t_l \in [t_0, t_f], k = 1, \dots, N-1, j = k+1, \dots, N$ . In Eq. 17,  $\mathcal{S}_{k_j i l}^*$  is the minimum separation (in terms of  $L_2$ -norm distance) reached by agents  $k^{th}$  and  $j^{th}$  on the uncontrolled trajectories generated at instants  $t_i$  and  $t_l$  respectively. Using Eq. 7, the instant  $t_{k_j i l}^*$  of minimum separation on the uncontrolled trajectories is computed as

$$t_{k_j i l}^*(\mathbf{c}_k(t_i), \mathbf{c}_j(t_l)) = \arg \min_{t \in [\max\{t_i, t_l\}, t_f + T]} \mathcal{S}_{k_j i l}(t) = \arg \min_{t \in [\max\{t_i, t_l\}, t_f + T]} \left\| \mathcal{S} (\boldsymbol{\psi}(t, \mathbf{c}_k(t_i)) - \boldsymbol{\psi}(t, \mathbf{c}_j(t_l))) \right\|_2 \quad (18)$$

As derived in Eq. 7 and 8,  $t_{k_j i l}^*$  is a function of the IC states at contingency instants. This makes  $\mathcal{S}_{k_j i l}^*$  a function of these IC states, and independent from the time along the uncontrolled trajectories. As highlighted in Remark II.2, this implies that safe separation all-along the uncontrolled trajectories is guaranteed by enforcing as many constraint as the number of contingency instants' combinations, i.e., once per each  $k_j i l$ -combination. As presented in Table 1 on the bottom and proved in Appendix VIII.A, this reduces the number of constraints required to enforce PS by one polynomial

degree of the number of discrete time samples. Specifically, from cubic to quadratic for each couple of active agents, and from quadratic to linear for each couple of active-permanently passive agents. Moreover, using the  $\mathcal{M}^*$ -formulation, the independency from the number of sample instants along the uncontrolled trajectories (i.e.,  $m$  on  $(t_f, t_f + T]$ ) makes the number of constraints required to enforce PS independent from the length of the PS horizon  $T$  itself. Figure 2 presents numerical examples of the trends in Table 1. To isolate the benefit of the  $\mathcal{M}^*$ -formulation, the number of agents is set to  $N_a = 2$  in Figures 2a-2b, and to  $N_a = N_p = 1$  in Figures 2c-2d, moreover for simplicity,  $m$  is set equal to  $n$ .

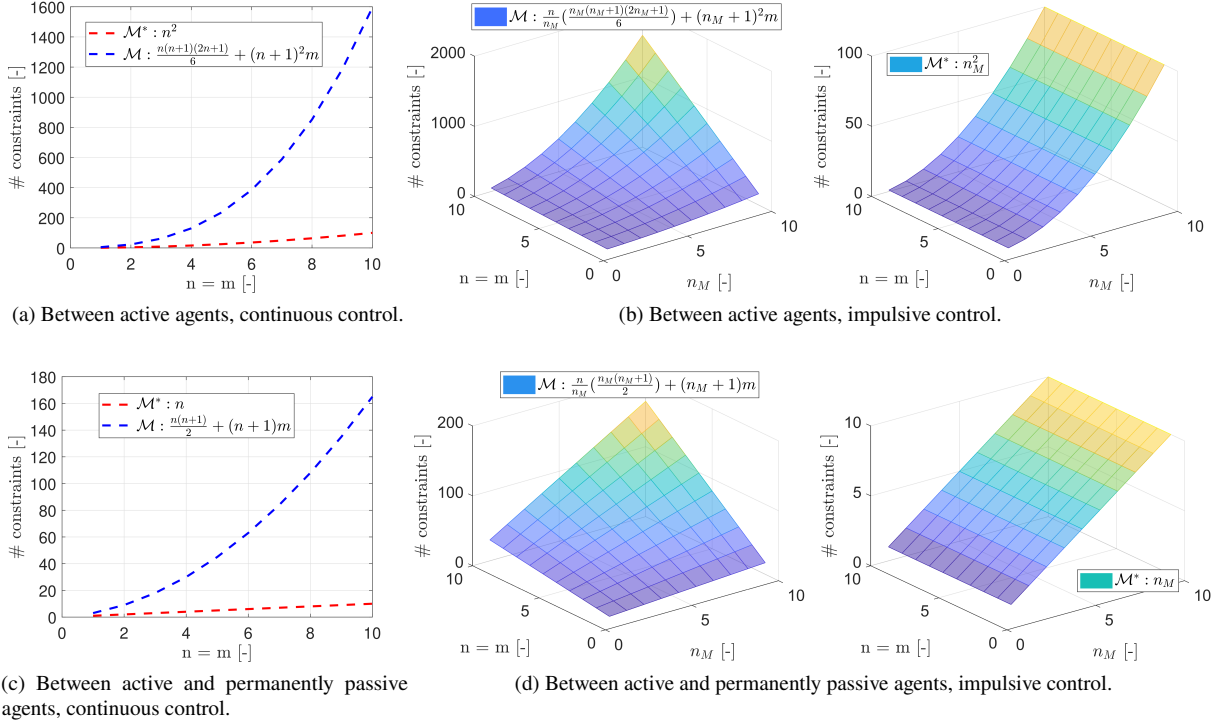


**Fig. 2** Number of constraints required to enforce PS as a function of the number of discrete time samples.

The  $\mathcal{M}^*$ -formulation assumes integrability of the dynamics after contingency, therefore, as presented in Section II, it requires the compensation of the effects of non-integrable dynamics and uncertainties within a bound defined as in Eq. 13. For multi-agent PS, let assume these effects can be superimposed as

$$\begin{aligned}
& \left| \frac{\partial \mathcal{M}^*(\mathbf{c}_k, \mathbf{c}_j)}{\partial \mathbf{c}_k} \Big|_{\tilde{\mathbf{c}}_k(t_i)} \int_{t_i}^{t_f+T} \tilde{\mathbf{d}}_c(\tau, \tilde{\mathbf{c}}_k(\tau)) d\tau \right| + \left| \frac{\partial \mathcal{M}^*(\mathbf{c}_k, \mathbf{c}_j)}{\partial \mathbf{c}_j} \Big|_{\tilde{\mathbf{c}}_j(t_i)} \int_{t_i}^{t_f+T} \tilde{\mathbf{d}}_c(\tau, \tilde{\mathbf{c}}_j(\tau)) d\tau \right| \\
& + \left| \frac{\partial \mathcal{M}^*(\mathbf{c}_k, \mathbf{c}_j)}{\partial \mathbf{c}_k} \Big|_{\tilde{\mathbf{c}}_k(t_i)} q \sqrt{\text{Diag} \left( \int_{t_i}^{t_f+T} \left( \tilde{\mathbf{D}}_c(\tau, \tilde{\mathbf{c}}_k(\tau)) \mathbf{C}_k(\tau) + \mathbf{C}_k(\tau) \tilde{\mathbf{D}}_c^T(\tau, \tilde{\mathbf{c}}_k(\tau)) + \mathbf{Q}_k(\tau) \right) d\tau + \mathbf{C}_k(t_i) \right)} \right| \\
& + \left| \frac{\partial \mathcal{M}^*(\mathbf{c}_k, \mathbf{c}_j)}{\partial \mathbf{c}_j} \Big|_{\tilde{\mathbf{c}}_j(t_i)} q \sqrt{\text{Diag} \left( \int_{t_i}^{t_f+T} \left( \tilde{\mathbf{D}}_c(\tau, \tilde{\mathbf{c}}_j(\tau)) \mathbf{C}_j(\tau) + \mathbf{C}_j(\tau) \tilde{\mathbf{D}}_c^T(\tau, \tilde{\mathbf{c}}_j(\tau)) + \mathbf{Q}_j(\tau) \right) d\tau + \mathbf{C}_j(t_i) \right)} \right| \leq \beta_{kjil}(t_i, t_l, T, q)
\end{aligned} \tag{19}$$

where  $\beta_{kjil} \in \mathbb{R}_{\geq 0}$ . Note that Eq. 19 assumes the capability of retrieving an estimate of both active and permanently passive agents' states through navigation and prediction. Using Eq. 19 and Eq. 17 evaluated at the mean IC states, Eq. 14 is specialized for multi-agent PS as

$$\mathcal{S}_{kjil}^*(\tilde{\mathbf{c}}_k(t_i), \tilde{\mathbf{c}}_j(t_l)) \geq \epsilon + \beta_{kjil}(t_i, t_l, T, q) \tag{20}$$

A graphical representation is provided in Figure 3. Assuming integrability of the dynamics after contingency,  $\mathcal{S}_{kjil}^*$  is the minimum separation between agents  $k^{th}$  and  $j^{th}$  who experienced control losses at instants  $t_i$  and  $t_l$  respectively. The bound  $\beta_{kjil}$  accounts for non-integrable dynamics and uncertainties effects on such minimum separation.

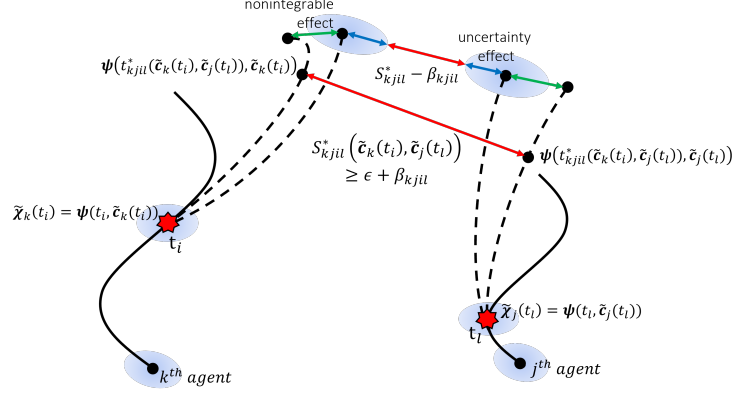


Fig. 3 Compensation of non-integrable dynamics and uncertainty within the efficient  $\mathcal{M}^*$ -formulation of PS.

### A. The Multi-agent Passively-Safe Optimal Control Problem

Given these developments, the multi-agent passively-safe OCP can be formulated efficiently as

#### Problem III.2.

$$\begin{aligned}
& \underset{\tilde{\mathbf{u}}_k(t)}{\text{minimize}} && \sum_{k=1}^{N_a} \int_{t_e}^{t_f} \mathcal{J}(\tilde{\mathbf{c}}_k(t), \mathbf{C}_k(t), \tilde{\mathbf{u}}_k(t), t) dt \\
& \text{subject to} && \dot{\tilde{\mathbf{c}}}_k(t) = \tilde{\mathbf{d}}_c(t, \tilde{\mathbf{c}}_k(t)) + \mathbf{B}_c(t, \tilde{\mathbf{c}}_k(t))\tilde{\mathbf{u}}_k(t) && \forall t \in [t_e, t_f], \quad k = 1, \dots, N_a \\
& && \dot{\tilde{\mathbf{c}}}_k(t) = \tilde{\mathbf{d}}_c(t, \tilde{\mathbf{c}}_k(t)) && \forall t \in [t_e, t_f], \quad k = 1, \dots, N_p \\
& && \dot{\mathbf{C}}_k(t) = \tilde{\mathbf{D}}_c(t, \tilde{\mathbf{c}}_k(t), \tilde{\mathbf{u}}_k(t))\mathbf{C}_k(t) + \mathbf{C}_k(t)\tilde{\mathbf{D}}_c^T(t, \tilde{\mathbf{c}}_k(t), \tilde{\mathbf{u}}_k(t)) + && \forall t \in [t_e, t_f], \quad k = 1, \dots, N_a \\
& && \quad \mathbf{B}_c(t, \tilde{\mathbf{c}}_k(t))\mathbf{U}_k(t)\mathbf{B}_c^T(t, \tilde{\mathbf{c}}_k(t)) + \mathbf{Q}_k(t) + \mathbf{E}_k(t) && \\
& && \dot{\mathbf{C}}_k(t) = \tilde{\mathbf{D}}_c(t, \tilde{\mathbf{c}}_k(t))\mathbf{C}_k(t) + \mathbf{C}_k(t)\tilde{\mathbf{D}}_c^T(t, \tilde{\mathbf{c}}_k(t)) + \mathbf{Q}_k(t) + \mathbf{E}_k(t) && \forall t \in [t_e, t_f], \quad k = 1, \dots, N_p \\
& && \mathcal{S}_{kji}^*(\tilde{\mathbf{c}}_k(t_i), \tilde{\mathbf{c}}_j(t_l)) \geq \epsilon + \beta_{kji}(t_i, t_l, T, q) && \forall t_i \in [t_e, t_f], \forall t_l \in [t_e, t_f], \\
& && && k = 1, \dots, N-1, \quad j = k+1, \dots, N \\
& && \tilde{\mathbf{u}}_k(t) \in \mathcal{U}_k && \forall t \in [t_e, t_f], \quad k = 1, \dots, N_a \\
& && \mathcal{N}(\tilde{\mathbf{c}}_k(t_f), \mathbf{C}_k(t_f)) \in \mathcal{C}_{k,f} && k = 1, \dots, N_a \\
& && \tilde{\mathbf{c}}_k(t_e) = \tilde{\mathbf{c}}_{k,e} \text{ and } \mathbf{C}_k(t_e) = \mathbf{C}_{k,e} && k = 1, \dots, N
\end{aligned} \tag{21}$$

Problem III.2 enforces PS, as in Definition III.1, over  $[t_e, t_f]$ ,  $\forall t_e \in [t_0, t_f]$ , at the cost of checking the reduced number of constraints presented in Table 1 on the bottom. From a practical implementation perspective, to achieve the envisioned reformulation of the PS constraint, the minimum separation  $\mathcal{S}_{kji}^*$  has to be computed as a function of the IC states at contingency instants. This requires the preliminary solution of the optimization problem in Eq. 18. In the following section, an algorithmic solution framework is presented. Finally, note that, if PS is enforced explicitly within the optimization problem, the trend of the number of required constraints is directly connected to the similar trend of the computational effort required to solve the optimization problem itself. Therefore the proposed efficient formulation is expected to provide benefits in terms of solution run-time. This is verified and analyzed in Section VI, applied to the solution of the passively-safe reconfiguration of VISORS [37].

## IV. Algorithmic Solution Framework

### A. Solution of the Centralized Problem

Problem III.2 is a non-convex centralized optimization problem. To solve it in a centralized fashion, various optimization algorithms can be used. Here a direct approach based on SCP is followed [23–25]. To apply SCP, non-convex constraints and cost function have to be linearized with respect to the previous solution in the series, defined as "SCP reference", and noted with  $(\cdot)$ :  $\{\tilde{\mathbf{c}}_k(t), \tilde{\mathbf{u}}_k(t)\}$ . Moreover, the optimization problem has to be time discretized.

To not replicate analysis already available in literature, and revisited by the authors too in [36], the focus here is on the newly formulated PS constraint. The turning point from an algorithmic perspective lies in the availability or not of an analytical expression of  $S_{kjil}^*$  as function of the IC. This is presented in Algorithm 1, and analyzed in the following.

---

**Algorithm 1:** Enforces PS on  $[t_0, t_f]$  for at least  $T$ , of at least  $\epsilon$ , at  $q$ - $\sigma$  confidence.

---

**Input:** Initial state estimate:  $\mathcal{N}(\bar{\mathbf{c}}_{k,0}, \mathbf{C}_{k,0})$ ,  $k = 1, \dots, N$ . Initial guess on:  $\{\bar{\mathbf{c}}_k(t_i), \bar{\mathbf{u}}_k(t_i)\}$ ,  $t_i \in [t_0, t_f]$ ,  $k = 1, \dots, N_a$ .  
**Output:**  $\bar{\mathbf{u}}_k(t_i)$ ,  $t_i \in [t_0, t_f]$ ,  $k = 1, \dots, N_a$ .  
**Data:**  $t_0, t_f, T, \epsilon, q, \mathbf{C}_{k,f}, MAX\_ITER$ , SCP parameters.

```

1 begin
2   for  $t_e = t_0$  to  $t_f$  do
3     Get  $\mathcal{N}(\bar{\mathbf{c}}_{k,e}, \mathbf{C}_{k,e})$ ,  $k = 1, \dots, N$ .
4      $\{\bar{\mathbf{c}}_k(t_i), \bar{\mathbf{u}}_k(t_i)\} \leftarrow \{\bar{\mathbf{c}}_k(t_i), \bar{\mathbf{u}}_k(t_i)\}$ ,  $t_i \in [t_e, t_f]$ ,  $k = 1, \dots, N_a$ 
5     if Closed-form expression of  $S_{kjil}^*$  is available then
6       Standard SCP, noting that  $\bar{\beta}_{kjil}$  in Eq. 22 can be precomputed at the reference.
7     else
8       Precompute  $\{\bar{r}_{kjil}^*, \bar{\beta}_{kjil}\}$  at the reference,  $\forall k, j, i, l$ .
9        $PS \leftarrow 0$ 
10      while SCP not converged or  $PS = 0$  do
11         $\overline{PS} \leftarrow 0$ ,  $ITER \leftarrow 0$ 
12        while  $\overline{PS} = 0$  and  $ITER < MAX\_ITER$  do
13          Solve Problem III.2, enforcing Eq. 23. Get  $\{\bar{\mathbf{c}}_k(t_i), \bar{\mathbf{u}}_k(t_i)\}$ ,  $t_i \in [t_e, t_f]$ ,  $k = 1, \dots, N_a$ .
14          Recompute  $\{t_{kjil}^*, \beta_{kjil}\}$  at the new solution,  $\forall k, j, i, l$ .
15          if  $S_{kjil}(t_{kjil}^*, \bar{\mathbf{c}}_k(t_i), \bar{\mathbf{c}}_j(t_l)) \geq \epsilon + \beta_{kjil}$ ,  $\forall k, j, i, l$  then
16             $\overline{PS} \leftarrow 1$ 
17             $\{\bar{r}_{kjil}^*, \bar{\beta}_{kjil}\} \leftarrow \{t_{kjil}^*, \beta_{kjil}\}$ ,  $\forall k, j, i, l$ .
18             $ITER \leftarrow ITER + 1$ 
19          if  $\overline{PS} = 0$  then
20            Select among the  $MAX\_ITER$  solutions computed the one that got closer to satisfy
21             $S_{kjil}(t_{kjil}^*, \bar{\mathbf{c}}_k(t_i), \bar{\mathbf{c}}_j(t_l)) \geq \epsilon + \beta_{kjil}$ ,  $\forall k, j, i, l$ .
22             $\{\bar{\mathbf{c}}_k(t_i), \bar{\mathbf{u}}_k(t_i)\} \leftarrow \{\bar{\mathbf{c}}_k(t_i), \bar{\mathbf{u}}_k(t_i)\}$ ,  $t_i \in [t_e, t_f]$ ,  $k = 1, \dots, N_a$ .
23            Recompute  $\{\bar{r}_{kjil}^*, \bar{\beta}_{kjil}\}$  at the new reference,  $\forall k, j, i, l$ .
24             $PS \leftarrow \overline{PS}$ 
25      Get  $\bar{\mathbf{u}}_k(t_e)$ ,  $k = 1, \dots, N_a$ .
26  return  $\bar{\mathbf{u}}_k(t_i)$ ,  $t_i \in [t_0, t_f]$ ,  $k = 1, \dots, N_a$ .

```

---

If an analytical expression of  $S_{kjil}^*$  is available, being in general a non-convex function of the IC state, it can be sequentially linearized around the SCP reference as

$$\frac{\partial S_{kjil}^*(\bar{\mathbf{c}}_k, \bar{\mathbf{c}}_j)}{\partial \bar{\mathbf{c}}_k} \Big|_{\bar{\mathbf{c}}_k(t_i), \bar{\mathbf{c}}_j(t_l)} (\bar{\mathbf{c}}_k(t_i) - \bar{\mathbf{c}}_k(t_i)) + \frac{\partial S_{kjil}^*(\bar{\mathbf{c}}_k, \bar{\mathbf{c}}_j)}{\partial \bar{\mathbf{c}}_j} \Big|_{\bar{\mathbf{c}}_k(t_i), \bar{\mathbf{c}}_j(t_l)} (\bar{\mathbf{c}}_j(t_l) - \bar{\mathbf{c}}_j(t_l)) + S_{kjil}^*(\bar{\mathbf{c}}_k(t_i), \bar{\mathbf{c}}_j(t_l)) \geq \epsilon + \bar{\beta}_{kjil} \quad (22)$$

where  $\bar{\beta}_{kjil}$  (defined in Eq. 19) is, by choice, directly evaluated at the reference. Since, from a PS enforcement perspective, the IC state covariances are used just to quantify this bound, this permits to: 1) pre-propagate them around the reference mean IC states and control inputs, 2) quantify  $\bar{\beta}_{kjil}$  evaluating the terms on the left-hand side of Eq. 19 at the reference, 3) enforce Eq. 22 within the optimization problem, without have to enforce explicitly the covariance dynamics constraint. This is an approximate but simpler solution than linearizing the terms on the left-hand side of Eq. 19. This approximation is the more accurate the better the SCP loop converges, and the closer the current solution is to the reference. The distance between the two is regulated through additional trust region constraints [23–25]. Note that the IC states of permanently passive agents at  $t_0$  can be treated as input parameters in the optimization, and not as optimization variables. This simplifies the left-hand side of Eq. 22 for active-permanently passive agents couples. In particular, the linearization with respect to the permanently passive agents' IC states is not performed.

If an analytical expression for  $\mathcal{S}_{kjiil}^*$  is not available, due to the fact that Eq. 18 is too complicated to be solved in closed-form, then an algorithmic development is needed. This is presented in Algorithm 1 (lines 9-24) and in the following. In particular, at each iteration of the SCP loop,  $\bar{t}_{kjiil}^*$  is precomputed at the reference through a simple search algorithm on the discretized interval  $[\max\{t_i, t_l\}, t_f + T]$ . Using Eq. 18, this search algorithm selects the discrete instant/index that minimizes  $\mathcal{S}_{kjiil}(t, \bar{\mathbf{c}}_k(t_i), \bar{\mathbf{c}}_j(t_l))$ , available as a closed-form expression of the reference mean IC states under assumption of integrability of the dynamics after contingency. Using the precomputed  $\bar{t}_{kjiil}^*$ , the PS constraint is enforced as

$$\left. \frac{\partial \mathcal{S}_{kjiil}(\bar{t}_{kjiil}^*, \bar{\mathbf{c}}_k, \bar{\mathbf{c}}_j)}{\partial \bar{\mathbf{c}}_k} \right|_{\bar{\mathbf{c}}_k(t_i), \bar{\mathbf{c}}_j(t_l)} (\bar{\mathbf{c}}_k(t_i) - \bar{\mathbf{c}}_k(t_i)) + \left. \frac{\partial \mathcal{S}_{kjiil}(\bar{t}_{kjiil}^*, \bar{\mathbf{c}}_k, \bar{\mathbf{c}}_j)}{\partial \bar{\mathbf{c}}_j} \right|_{\bar{\mathbf{c}}_k(t_i), \bar{\mathbf{c}}_j(t_l)} (\bar{\mathbf{c}}_j(t_l) - \bar{\mathbf{c}}_j(t_l)) + \mathcal{S}_{kjiil}(\bar{t}_{kjiil}^*, \bar{\mathbf{c}}_k(t_i), \bar{\mathbf{c}}_j(t_l)) \geq \epsilon + \bar{\beta}_{kjiil} \quad (23)$$

With arguments similar to the one used for the standard collision avoidance in [30], it is possible to prove that Eq. 23 represents a sufficient condition for the satisfaction of  $\mathcal{S}_{kjiil}(\bar{t}_{kjiil}^*, \bar{\mathbf{c}}_k(t_i), \bar{\mathbf{c}}_j(t_l)) \geq \epsilon + \bar{\beta}_{kjiil}$ . The formal proof is revisited by the authors in [34, 36], and omitted here for compactness. Nevertheless, Eq. 23 does not constitute a sufficient condition of having the actual minimum separation at  $t_{kjiil}^*$  being greater than  $\epsilon + \bar{\beta}_{kjiil}$ . This is represented graphically in Figure 4a. At the SCP reference, minimum separation on the uncontrolled trajectories is reached at instant  $\bar{t}_{kjiil}^*$ . At the current solution, at instant  $t_{kjiil}^*$  the separation reached at instant  $t_{kjiil}^*$  by the current solution may be larger than the minimum one since  $t_{kjiil}^* \neq \bar{t}_{kjiil}^*$ . Therefore,  $\bar{t}_{kjiil}^*$  has to be sequentially updated within the SCP

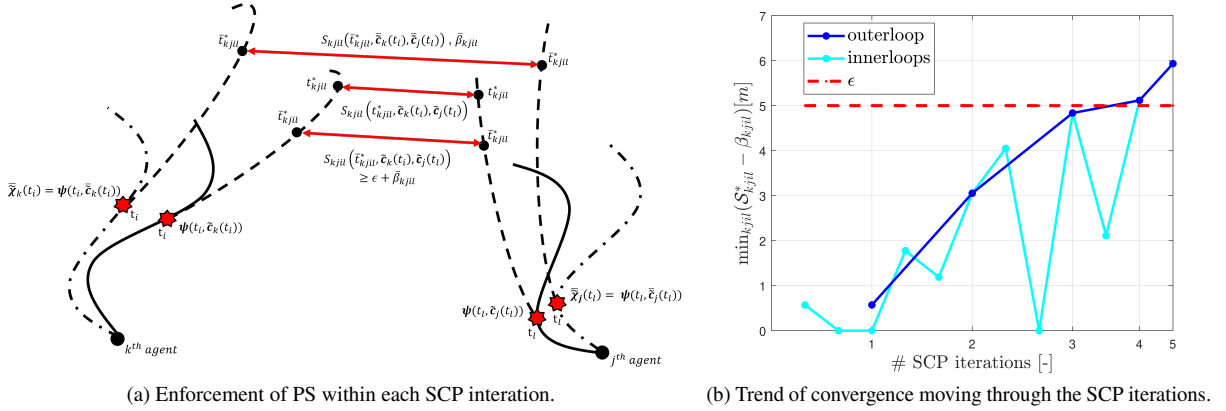


**Fig. 4 Enforcement of PS within the SCP pipeline.**

pipeline to guarantee that, at convergence, the actual worst case minimum separation is constrained. In particular, 1) the optimization problem is solved by enforcing Eq. 23 which uses  $\bar{t}_{kjiil}^*$  and  $\bar{\beta}_{kjiil}$  evaluated at the reference, then 2)  $t_{kjiil}^*$  and  $\beta_{kjiil}$  are computed at the new solution, then 3) the actual minimum separation  $\mathcal{S}_{kjiil}(t_{kjiil}^*, \bar{\mathbf{c}}_k(t_i), \bar{\mathbf{c}}_j(t_l))$  is checked a-posteriori to be  $\geq$  than  $\epsilon + \beta_{kjiil}$ . If this condition is true, the algorithm proceeds to the next SCP-loop iteration, if it is not true, the optimization problem is solved again keeping the same linearization reference but using the newly computed  $t_{kjiil}^*$  and  $\beta_{kjiil}$ . Such inner-loop brakes either if PS is satisfied a-posteriori, or if a maximum number of iterations ( $MAX\_ITER \in \mathbb{N}_{>0}$ ) is reached. If the maximum number of iterations is reached, the solution in the inner-loop that got closer to satisfying PS is taken as reference and the algorithm proceeds to the subsequent iteration of the SCP. Introducing a maximum number of iterations in the inner-loop prevents the algorithm to get stuck into intermediate solutions, in which the PS constraint does not get satisfied in few iterations. Figure 4b, presents a sample trend of convergence to a feasible passively-safe solution (with  $\epsilon = 5\text{m}$ ) moving through the inner-loops of Algorithm 1 (lines 12-18, light-blue line, with  $MAX\_ITER = 3$ ) and the SCP outer-loop (blue line). Moreover, a condition on the convergence of the whole SCP algorithm is introduced. Beside the satisfaction of its stopping criteria, the SCP algorithm is considered converged only if the final solution out of the SCP loop is passively-safe. Otherwise, the problem is deemed unfeasible.

The feasibility of finding a passively-safe solution trajectory depends on various factors, as for example, the boundary conditions, the level of uncertainty present in the system (which influences the size of the PS bounds), optimization parameters as the initial warm-starting trajectory, the defined time discretization (or the number of candidate maneuvers considered), trust regions, etc. Certain optimization parameters can be properly selected and tuned to increase the

chances of finding a feasible solution. Other factors as the boundary conditions or the level of uncertainty are defined given the system and control scenario. Therefore, given a certain system, control scenario and optimization set-up, the possibility of not finding a feasible passively-safe solution is present. In risk sensitive applications, if a feasible solution is repeatedly not found, it is necessary to have a logic that falls back on an alternative action. For DSS, this alternative action can be for example a reactive or proactive approach to collision avoidance.

Both if  $\mathcal{S}_{k,jil}^*$  is available in closed-form and not, Eq. 22 and 23 enforce the reduced number of constraints presented in Table 1 on the bottom. This possibly cuts the computational expense, and increases the chances of converging in useful time to a feasible solution using off-the-shelf solvers [38, 39]. As final mention, as in any SCP algorithm, to implement Algorithm 1 an initial "warm-start" guess on the profile:  $\{\tilde{\mathbf{c}}_k(t_i), \tilde{\mathbf{u}}_k(t_i)\}, \forall ki$ , is required as input. Such initial guess does not have to be feasible, i.e., it does not have to satisfy the PS constraint. An option is to initialize the algorithm with a profile that simply solves for the two-point-boundary-value-problem from initial to final conditions, or better, that satisfies the standard collision avoidance constraint but is not passively-safe. Obviously, the computational effort is reduced if a sub-optimal passively-safe solutions is already available, as analyzed in Section VI.

## B. Decentralization

In a multi-agent setting, solving Problem III.2 using Algorithm 1 at each  $t_e \in [t_0, t_f]$  requires: 1) the communication of the state estimates of each agent to the one assigned with the role of computing the centralized plan, 2) the communication back to each agent of the newly computed plan. From an operational stand-point may be beneficial the computation of the centralized plan at the initial instant  $t_0$  and then at subsequent instants  $t_e$  just upon necessity. This subtend the need of complementing the centralized problem with an additional decentralized optimization problem, defined conventionally as the "tracking problem". This enables each agent to independently compute a "tracking control plan" that tracks a previously computed centralized plan, any time an updated state estimate is available. The tracking problem has to compensate for the presence of initial tracking errors, as well as for the acting dynamics, while reinforcing guarantees of constraints satisfaction. In [36], the authors present a possible formulation of the tracking problem, as well as the logic regulating the interplay between centralized and decentralized problems solution. Here, for compactness, just the key aspects are summarized. Let introduce the superscript  $(.)^{\mathcal{G}}$  to indicate variables associated to the centralized "guidance" and the superscript  $(.)^{\mathcal{T}}$  to indicate variables associated to the decentralized "tracking". Algorithm 1 is used at  $t_0$  to produce the centralized plan  $\{\tilde{\mathbf{u}}_k^{\mathcal{G}}(t), \tilde{\mathbf{c}}_k^{\mathcal{G}}(t), \mathbf{C}_k^{\mathcal{G}}(t)\}, \forall t \in [t_0, t_f]$ , for each active agent. If feasible, the centralized plan is certified as passively-safe. At each instant  $t_e$ , each agent acquires a state estimate  $\mathcal{N}(\tilde{\mathbf{c}}_{k,e}, \mathbf{C}_{k,e})$ . Given this estimate and the available centralized plan, a tracking error is possibly present and defined as  $\tilde{\mathbf{c}}_k^{\mathcal{T}}(t_e) = \tilde{\mathbf{c}}_{k,e} - \tilde{\mathbf{c}}_k^{\mathcal{G}}(t_e)$ . This tracking error propagates through the dynamics of the system. In addition, the newly estimated covariance  $\mathbf{C}_{k,e}$  is not necessarily equal to the one predicted during the solution of the centralized problem, and used to evaluate the bounds in Eq. 22 and 23. To make the guidance plan robust to these tracking effects, the idea is to enlarge the bound used at guidance level by an additional margin. In particular, for each involved agent, the following term can be added to the left-hand side of Eq. 19:  $|(\partial \mathcal{M}^* / \partial \mathbf{c}_k) |_{\tilde{\mathbf{c}}_k(t_i)} \cdot \mathbf{v}_{ki}^{\mathcal{T}}|$ . Where,  $\mathbf{v}_{ki}^{\mathcal{T}} \in \mathbb{R}_{\geq 0}^s$  is a constant total worst-case tracking error which is then reinforced at tracking level on the mean tracking state as

$$|\tilde{\mathbf{c}}_k^{\mathcal{T}}(t_i)| + \boldsymbol{\beta}_{ki}^{\mathcal{T}} \leq \mathbf{v}_{ki}^{\mathcal{T}} \quad (24)$$

$\forall t_i \in [t_0, t_f]$ , for  $k = 1, \dots, N_a$ . In Eq. 24,  $\boldsymbol{\beta}_{ki}^{\mathcal{T}} \in \mathbb{R}_{\geq 0}^s$  is quantified such that

$$\boldsymbol{\beta}_{ki}^{\mathcal{T}} \geq \left| \int_{t_i}^{t_f+T} \tilde{\mathbf{a}}_c(\tau, \tilde{\mathbf{c}}_k(\tau)) d\tau - \int_{t_i}^{t_f+T} \tilde{\mathbf{a}}_c(\tau, \tilde{\mathbf{c}}_k^{\mathcal{G}}(\tau)) d\tau \right| + q \sqrt{\left| \text{Diag} \left( \int_{t_i}^{t_f+T} (\tilde{\mathbf{D}}_c(\tau, \tilde{\mathbf{c}}_k(\tau)) \mathbf{C}_k(\tau) + \mathbf{C}_k(\tau) \tilde{\mathbf{D}}_c^T(\tau, \tilde{\mathbf{c}}_k(\tau)) + \mathbf{Q}_k(\tau)) d\tau + \mathbf{C}_k(t_i) \right) \right| - q \sqrt{\left| \text{Diag} \left( \int_{t_i}^{t_f+T} (\tilde{\mathbf{D}}_c(\tau, \tilde{\mathbf{c}}_k^{\mathcal{G}}(\tau)) \mathbf{C}_k^{\mathcal{G}}(\tau) + \mathbf{C}_k^{\mathcal{G}}(\tau) \tilde{\mathbf{D}}_c^T(\tau, \tilde{\mathbf{c}}_k^{\mathcal{G}}(\tau)) + \mathbf{Q}_k^{\mathcal{G}}(\tau)) d\tau + \mathbf{C}_k^{\mathcal{G}}(t_i) \right) \right|}} \quad (25)$$

to capture the net effect of tracking on the non-integrable and uncertainty effects quantified at guidance level. In particular, in Eq. 25, the non superscripted state quantities refer to the ones computed at tracking level, which depend on the tracking error itself.

Finally, a high-level logic regulating the interplay between guidance and tracking is implemented. Specifically, at every instant  $t_e$  an updated state estimate is available, the system has two options: a) tracking the centralized plan or, b) recomputing the centralized plan. The high-level logic has to decide autonomously on-board between a) or b). The triggers in this decision are mainly two: 1) the feasibility of the tracking, and 2) the prediction that the currently planned control solution leads to constraints satisfaction, given the latest state estimate and the on-board knowledge of the system dynamics. Therefore, at each instant  $t_e$ , each agent acquires an updated state estimate and tracks. If for some agents, the

tracking is not feasible the agent(s) share the information and the "planner agent" recomputes the centralized plan using the latest state estimates. If the tracking is feasible for everyone, the agent(s) share their updated state estimates and the corrected control plans to the planner agent, which does a sanity-check. In particular, it propagates in open-loop both mean and covariance trajectories of each agent starting at the newly acquired state estimates using the corrected control plans that has been communicated. This open-loop propagation permits to check if the expected worst case minimum separations reached on the uncontrolled trajectories are actually greater than  $\epsilon$ . If any of them is not greater than  $\epsilon$ , PS is not guaranteed by the current control plan given the newly acquired state estimate. Therefore, the centralized plan must be recomputed. Otherwise, if all of them are greater than  $\epsilon$ , the agents receive the go ahead to actuate the corrected control plan. This sanity-check performed by the planner agent introduces delay and computational overhead in the control pipeline, requiring the communication back and forth of data between agents as well as the open-loop propagation needed for checking the minimum separations. Depending on the risk sensitivity of the control scenario it is possible to skip this sanity-check or perform it just at key instants of the multi-agent reconfiguration (e.g., after a largely uncertain maneuver actuated by an agent). If the sanity-check is not performed, the only decision trigger on recomputing the centralized plan or not remains the possible unfeasibility of the tracking.

## V. Application to Distributed Space Systems

The orbital motion of a  $N$ -spacecraft DSS can be described either by  $N$  orbits in inertial space around the main attractor or by one reference orbit, either virtual or occupied by a chief spacecraft, and by  $N$  (or  $N - 1$ ) relative trajectories with respect to this reference. These two ways of modeling the spacecraft motion influence the structure of the governing ODE, and therefore give rise to two different ways of applying VoP and the framework proposed in Sections II-IV. As described in the introduction, one approach uses the OE as IC state, while the other approach uses the ROE. From an operational stand-point, for spacecraft in closed proximity, modeling directly the relative motion is advantageous both from a dynamics modeling standpoint [18–21] and navigation accuracy standpoint [40]. In particular, about the latter, spacecraft absolute motion navigation solutions are less accurate than relative motion ones, usually by at least one order of magnitude. Navigation accuracy plays a fundamental role in the developed framework, since it determines the level of uncertainty present, and in face of which PS guarantees have to be provided (see Eq. 19). Too high uncertainty entails high chance of unfeasibility in finding a passively-safe control solution. This is analyzed in the test cases in Section VI.

Following the relative motion approach, the reference orbit is uniquely defined by a set of OE:  $\boldsymbol{\alpha} \in \mathbb{R}^6$ . Let us use the quasi non-singular OE definition [13]:  $\boldsymbol{\alpha} = \{a, \lambda_\nu, e_x, e_y, i, \Omega\}$ , with  $a$  the semi-major axis,  $\lambda_\nu = \nu + \omega$  the true argument of latitude,  $\nu$  the true anomaly,  $\omega$  the argument of perigee,  $\{e_x, e_y\} = \{e \cos(\omega), e \sin(\omega)\}$  the eccentricity vector,  $e$  the eccentricity,  $i$  the inclination, and  $\Omega$  the right ascension of the ascending node. The  $N$  (or  $N - 1$ ) relative trajectories are defined by the relative Cartesian state expressed in the radial/along-track/normal (RTN) [13] frame centered on the reference, as  $\boldsymbol{\chi}_k = \{\delta \mathbf{r}_k, \delta \dot{\mathbf{r}}_k\} \in \mathbb{R}^6$ , for  $k = 1, \dots, N$ , where  $\delta \mathbf{r}_k \in \mathbb{R}^3$  and  $\delta \dot{\mathbf{r}}_k \in \mathbb{R}^3$  are correspondingly the relative position and velocity of the  $k^{th}$  spacecraft. The dynamics of  $\boldsymbol{\chi}_k$  is governed by a nonlinear ODE [41]

$$\dot{\boldsymbol{\chi}}_k(t) = \mathbf{z}(\boldsymbol{\chi}_k(t)) + \mathbf{p}(\boldsymbol{\chi}_k(t)) + \mathbf{B}\mathbf{u}_k(t) \quad (26)$$

where,  $\mathbf{z} \in \mathbb{R}^6$  models the relative effect of two-body spherical gravity as well as Euler, centrifugal and Coriolis accelerations raising from the non-inertial (and potentially perturbed) nature of the rotating RTN frame,  $\mathbf{p} \in \mathbb{R}^6$  models the differential effect of orbital perturbations, and  $\mathbf{u}_k \in \mathbb{R}^3$  is the  $k^{th}$  spacecraft control acceleration expressed in RTN frame, with  $\mathbf{B} = [\mathbf{0}_{3 \times 3}; \mathbf{I}_{3 \times 3}] \in \mathbb{R}^{6 \times 3}$  the control input matrix. Although the relative dynamics in Eq. 26 depends on the reference OE, this dependence is let implicit in the notation for compactness. In literature, analytical solutions for the homogeneous nonlinear part of Eq. 26 are not available. Nevertheless, linearizing the differential spherical gravity terms in  $\mathbf{z}$  for small spacecraft separations, Eq. 26 is rewritten exactly as

$$\dot{\boldsymbol{\chi}}_k(t) = \mathbf{A}(t)\boldsymbol{\chi}_k(t) + \mathbf{d}(\boldsymbol{\chi}_k(t)) + \mathbf{B}\mathbf{u}_k(t) \quad (27)$$

where  $\mathbf{A} \in \mathbb{R}^{6 \times 6}$  is the linear(ized) integrable part, and  $\mathbf{d} \in \mathbb{R}^6$  is the nonlinear non-integrable part, which contains both  $\mathbf{p}$  and the truncated higher-order terms of  $\mathbf{z}$ . Since the beginning of spaceflight, solutions for the linear part of Eq. 27 have been developed by different authors. For example, Hill, Clohessy and Wiltshire (HCW) developed a famous solution for spacecraft in near-circular orbits [14], whereas Yamanaka and Ankersen (YA) for spacecraft in eccentric orbits [16]. All these solutions share common structure:  $\boldsymbol{\chi}_k(t) \approx \boldsymbol{\Psi}(t)\mathbf{c}_k$ , where,  $\mathbf{c}_k = \{c_{1,k}, c_{2,k}, c_{3,k}, c_{4,k}, c_{5,k}, c_{6,k}\} \in \mathbb{R}^6$  is the  $k^{th}$  spacecraft IC state, and  $\boldsymbol{\Psi}$  is the fundamental matrix solution of the linear ODE. Such fundamental matrix depends on time, usually through the reference orbit's true anomaly  $\nu = \nu(t)$ , but does not depend on the IC since the integrated

ODE is linear. In this paper, the chosen IC state is a tuned version of the YA's IC. The associated  $\Psi$  is presented in Eq. 37 in Appendix VIII.B as a function of the reference OE.  $\mathbf{c}_k$  is non-dimensional, which makes the first three rows of  $\Psi$  having dimension of length, and the last three rows of length over time.  $\Psi$  models both bounded periodic motion and unbounded (unstable) motion. If  $c_{1,k} \neq 0$ , the motion is unstable in both along-track and radial direction if the reference orbit is eccentric, or just in along-track direction if the orbit is near-circular. If  $c_{1,k} = 0$  the motion is bounded and periodic. As mentioned, the relative motion IC can be mapped at the first-order to a set of ROE, linear or nonlinear combination of the OE of two spacecraft or of a reference and a spacecraft. Eq. 38 in Appendix VIII.B provides a linear map between the used IC and the quasi-nonsingular ROE.

### A. Closed-form solutions of Passive Safety in Eccentric Orbits

Closed-form analysis aims at computing an analytical expression of  $\mathcal{S}_{kjil}^*$ , or of a lowerbound  $\underline{\mathcal{S}}_{kjil}^* \leq \mathcal{S}_{kjil}^*$ , as function of the IC. To that end, Eq. 18 has to be solved analytically using  $\Psi$  in Eq. 37 in Appendix VIII.B. The full 3-D solution for relative motion in eccentric orbit accounting for both bounded and unbounded motion is rather complicated. Therefore, literature [6, 11] has been developing reduced solutions by: 1) assuming  $c_{1,k} \sim 0, \forall k$ , and so enforcing the relative motion bounded and periodic for all spacecraft, 2) decomposing the full 3-D problem in two 2-D sub-problems (RN and RT), 3) assuming near-circular orbits. In this section, the third assumption is removed, and two analytical lowerbounds,  $\underline{\mathcal{S}}_{kjil}^{*RN}$  and  $\underline{\mathcal{S}}_{kjil}^{*RT}$ , are computed for relative motion in eccentric orbits for the first time. Here, the superscripts RN/RT refer to the sub-planes in which the minimum separation is computed. To that end, for compactness, let us use the notations  $\mathbf{c}_{kjil} = \mathbf{c}_k(t_i) - \mathbf{c}_j(t_l)$  and  $\epsilon_{kjil} = \epsilon + \beta_{kjil}$ . Assuming  $c_{1,k} \sim 0$  and using Eq. 37, the first three components of  $\Psi(t)\mathbf{c}_{kjil}$  are

$$\begin{aligned} \delta r_{R,kjil}(t) &\approx -ac_{34,kjil} \cos(\lambda_v(t) - \theta_{34,kjil}) \\ \delta r_{T,kjil}(t) &\approx \frac{1}{\rho(v(t))} ac_{2,kjil} + \left( \frac{1}{\rho(v(t))} + 1 \right) ac_{34,kjil} \sin(\lambda_v(t) - \theta_{34,kjil}) \\ \delta r_{N,kjil}(t) &\approx \frac{1}{\rho(v(t))} ac_{56,kjil} \sin(\lambda_v(t) - \theta_{56,kjil}) \end{aligned} \quad (28)$$

which represents the relative position of  $k^{th}$  and  $j^{th}$  spacecraft along the uncontrolled trajectories generated by control losses at instant  $t_i$  and  $t_l$  respectively, assuming the integrability of the dynamics after contingency. In Eq. 28, the IC state has been expressed in polar form  $\mathbf{c}_{ab,kjil} = \{c_{a,kjil}, c_{b,kjil}\} = c_{ab,kjil} \{\cos(\theta_{ab,kjil}), \sin(\theta_{ab,kjil})\}$ . Looking at Eq. 28, the terms function of  $\rho(v(t))$  hinder a clear geometrical interpretation of the relative motion. In particular,  $\rho(v) = 1 + e \cos(v) \in [1 - e, 1 + e]$ , where the two extreme values are achieved at the apogee and at the perigee of the eccentric orbit respectively. If  $\rho(v)$  is fixed to  $\bar{\rho} \in [1 - e, 1 + e]$ , Eq. 28 has geometrical representation as in Fig. 5. Such representation is not the real relative motion in eccentric orbit, which includes  $\rho(v)$  as a time varying function of

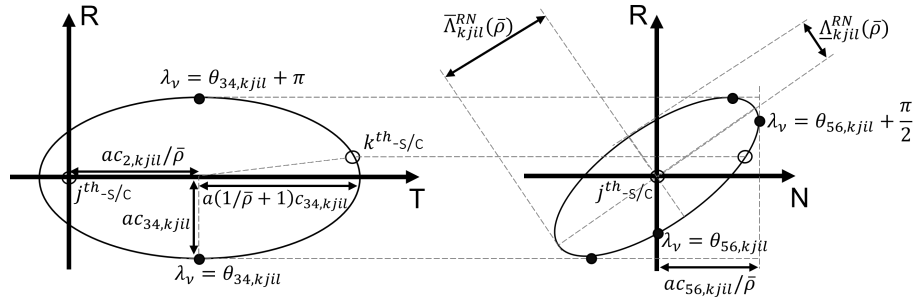


**Fig. 5 Geometrical representation of Eq. 28, fixing  $\rho(v(t)) = \bar{\rho}$ . In near-circular orbit, being  $\rho(v(t)) \approx 1 \forall t$ , it becomes the true representation of the relative motion.**

the true anomaly. On the other hand, at each  $v(t) = \bar{v}$ , the real relative motion trajectory is tangent to the ellipses in Fig. 5 at the point  $\lambda_v = \omega + \bar{v}$ , with  $\bar{\rho} = 1 + e \cos(\bar{v})$ . This implies that, a lowerbound of the real separation between spacecraft on the uncontrolled trajectories can be computed in either RN or RT planes by evaluating the minimum separations of the two ellipses from the origin. As presented in the following, these minimum separations assume extremal values at the perigee and apogee of the eccentric orbit. The minima of these extremals are by definition

lowerbounds of  $\mathcal{S}_{kjil}^*$ , and can be used in Eq. 20 to achieve PS. Being the uncontrolled relative motion assumed bounded and periodic ( $c_{1,k} \sim 0$ ), PS is achieved infinitely ( $T=\infty$ ). Note that, if such assumption is too limiting for a specific application, it can be avoided by following the numerical path to  $l_{kjil}^*$  computation presented in Algorithm 1 (lines 9-24).

### 1. Passive Safety in RN-plane

The minimum separation of the RN ellipse from the origin is computed as the minimum eigenvalue  $\underline{\Delta}_{kjil}^{RN}(\bar{\rho})$  of a singular value decomposition (Fig. 5, right) as

$$\underline{\mathcal{S}}_{kjil}^{*RN}(\bar{\rho}) = \frac{\sqrt{2}a \left| c_{34,kjil} \cdot \frac{c_{56,kjil}}{\bar{\rho}} \right|}{\left[ (c_{34,kjil})^2 + \left( \frac{c_{56,kjil}}{\bar{\rho}} \right)^2 + \left| c_{34,kjil} + \frac{c_{56,kjil}}{\bar{\rho}} \right| \cdot \left| c_{34,kjil} - \frac{c_{56,kjil}}{\bar{\rho}} \right| \right]^{1/2}} \quad (29)$$

Consistently with Remark II.2,  $\underline{\mathcal{S}}_{kjil}^{*RN}(\bar{\rho})$  is, for a fixed value of  $\bar{\rho}$ , independent from time and function of the IC states evaluated at the contingency instants. Taking the partials with respect to  $\bar{v}$ , its smallest and largest values are achieved correspondingly at the perigee and apogee of the eccentric orbit. Therefore, a lowerbound over the full orbit is obtained substituting  $\bar{\rho}$  with  $1+e$ . Using Eq. 29, the sufficient condition of PS in Eq. 20 can be rewritten as

$$\left| \hat{c}_{34,kjil} \cdot \hat{c}_{56,kjil} \right| = \left| \cos(\theta_{34,kjil} - \theta_{56,kjil}) \right| \geq \cos(\xi_{kjil}(\bar{\rho})) \quad (30)$$

with

$$\cos(\xi_{kjil}(\bar{\rho})) = \frac{\epsilon_{kjil}\bar{\rho}}{ac_{34,kjil}c_{56,kjil}} \sqrt{(c_{34,kjil})^2 + \left( \frac{c_{56,kjil}}{\bar{\rho}} \right)^2 - \frac{(\epsilon_{kjil})^2}{a^2}} \quad (31)$$

$\forall t_i \in [t_0, t_f], \forall t_l \in [t_0, t_f]$ , for  $k = 1, \dots, N-1, j = k+1, \dots, N$ . Here,  $c_{ab,kjil} = c_{ab,kjil}\hat{c}_{ab,kjil}$ . Eq. 30-31 have an interesting geometrical interpretation in IC space, as presented in Fig. 6a. In particular, to maintain PS in RN-plane the phase angle between the vectors  $c_{34,kjil}$  and  $c_{56,kjil}$ , i.e.  $\theta_{34,kjil} - \theta_{56,kjil}$ , must be either contained in the interval  $[-\xi_{kjil}(\bar{\rho}), \xi_{kjil}(\bar{\rho})]$  (parallel configuration) or in the interval  $[\pi - \xi_{kjil}(\bar{\rho}), \pi + \xi_{kjil}(\bar{\rho})]$  (anti-parallel configuration), where the most and least tight conditions are achieved correspondingly at the perigee and apogee of the eccentric orbit. Eq. 30-31 represent the  $c_{34}/c_{56}$ -separation concept, which in near-circular orbit, using ROE, becomes the relative eccentricity/inclination-separation concept [6], used for the relative orbit design in the GRACE, TANDEM-X, PRISMA and BIROS missions flown in LEO [10].

### 2. Passive Safety in RT-plane

The minimum separation of the RT ellipse from the origin is computed solving analytically Eq. 18 formulated as a function of  $\lambda_r(t)$ , by using Eq. 28 and fixing  $\bar{\rho}$ . The resulting minimum separation is

$$\underline{\mathcal{S}}_{kjil}^{*RT}(\bar{\rho}) \begin{cases} = a\frac{1}{\bar{\rho}}c_{2,kjil} - a\left(\frac{1}{\bar{\rho}} + 1\right)c_{34,kjil} & \text{not-encircling} \\ = \begin{cases} \sqrt{a^2c_{34,kjil}^2 - \frac{1}{1+2\bar{\rho}}a^2c_{2,kjil}^2} & \frac{\epsilon_{kjil}}{a} \leq c_{34,kjil} < \frac{1+\bar{\rho}}{\bar{\rho}} \frac{\epsilon_{kjil}}{a} \\ a\left(\frac{1}{\bar{\rho}} + 1\right)c_{34,kjil} - a\frac{1}{\bar{\rho}}c_{2,kjil} & c_{34,kjil} \geq \frac{1+\bar{\rho}}{\bar{\rho}} \frac{\epsilon_{kjil}}{a} \end{cases} & \text{encircling} \end{cases} \quad (32)$$

where "not-encircling" refers to Fig. 6b, top left, whereas, "encircling" refers to Fig. 6b, center and bottom left. Consistently with Remark II.2,  $\underline{\mathcal{S}}_{kjil}^{*RT}(\bar{\rho})$  is, for a fixed value of  $\bar{\rho}$ , independent from time and function of the IC states evaluated at the contingency instants. Taking the partials with respect to  $\bar{v}$ , its smallest and largest values are achieved correspondingly at the perigee and apogee of the eccentric orbit for the not-encircling case, and at the apogee and perigee for the encircling case. Therefore, a lowerbound over the full orbit can be obtained by substituting  $\bar{\rho}$  with  $1+e$  for the not-encircling case, whereas with  $1-e$  for the encircling case. Using Eq. 32, the sufficient condition of PS in Eq. 20 can be rewritten as

$$|c_{2,kjil}| \begin{cases} \geq (1+\bar{\rho})c_{34,kjil} + \frac{\epsilon_{kjil}}{a} & \text{not-encircling} \\ \leq \begin{cases} \sqrt{(1+2\bar{\rho})\left(c_{34,kjil}^2 - \frac{(\epsilon_{kjil})^2}{a^2}\right)} & \text{if } \frac{\epsilon_{kjil}}{a} \leq c_{34,kjil} < \frac{1+\bar{\rho}}{\bar{\rho}} \frac{\epsilon_{kjil}}{a} \\ (1+\bar{\rho})c_{34,kjil} - \frac{\epsilon_{kjil}}{a} & \text{if } c_{34,kjil} \geq \frac{1+\bar{\rho}}{\bar{\rho}} \frac{\epsilon_{kjil}}{a} \end{cases} & \text{encircling} \end{cases} \quad (33)$$

$\forall t_i \in [t_0, t_f], \forall t_l \in [t_0, t_f]$ , for  $k = 1, \dots, N-1, j = k+1, \dots, N$ . In IC space, Eq. 33 has representation as in Fig. 6b, right, where the most tight and least tight conditions are achieved correspondingly at the perigee and apogee for the not-encircling case, and at the apogee and perigee for the encircling case. In near-circular orbit, using ROE, Eq. 33 reduces to the solutions in [11].

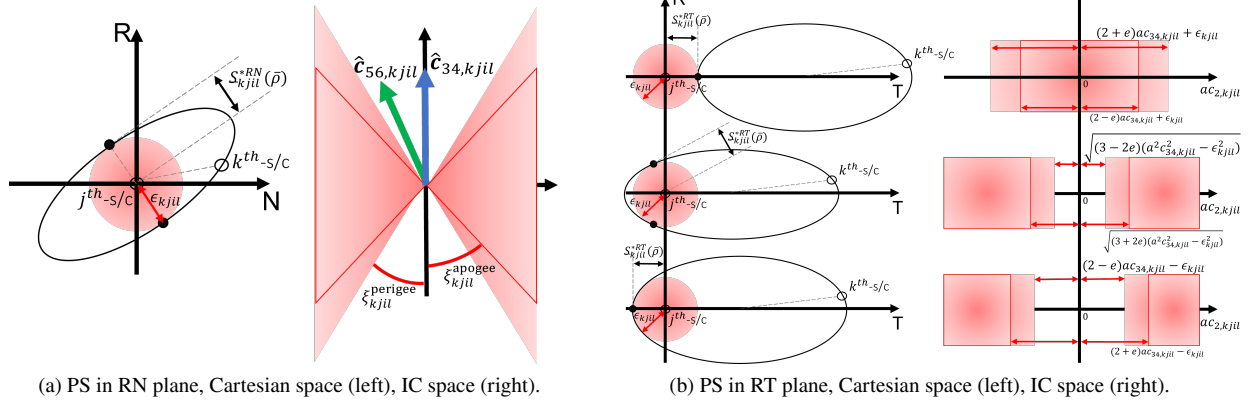


**Fig. 6** Graphical representation of the sufficient conditions of PS in eccentric orbits.

## B. Eccentric Swarms Designs

The newly derived analytical PS conditions in RN and RT planes permit to generalize the spacecraft swarm designs developed in [11] from near-circular orbits to eccentric orbits. The "high-density" swarm design is defined such that all spacecraft are distributed at equal distance in the  $c_{34}$ -plane and RT PS is achieved by enforcing sufficient separation in along-track direction through Eq. 33. To do so, let design the swarm such that:  $c_{1,k} = 0$ , and  $c_{34,kj} = \|c_{34,k} - c_{34,j}\|_2 \geq c_{34,min} \geq \epsilon/a$ . Moreover, all spacecraft are distributed at equal distance ( $c_{34,min}$ ) in the  $c_{34}$ -plane as

$$c_{34,k} = \begin{pmatrix} c_{34,min} \left( W_k \cos(\theta_{34}^{hd}) + X_k \cos(\theta_{34}^{hd} + \frac{\pi}{3}) \right) \\ c_{34,min} \left( W_k \sin(\theta_{34}^{hd}) + X_k \sin(\theta_{34}^{hd} + \frac{\pi}{3}) \right) \end{pmatrix} \quad (34)$$

where, the angular phase  $\theta_{34}^{hd}$  is selected to arrange the spacecraft in the plane, and  $W_k$  and  $X_k$  are not-simultaneously zero integers, that cannot simultaneously satisfy  $W_k = W_j$  and  $X_k = X_j$ , for any  $k \neq j$ . Given this design, by noticing that  $|c_{2,kj}| \leq |c_{2,k}| + |c_{2,j}|$ , RT PS is enforced for the entire swarm by using Eq. 33 evaluated at the apogee (most tight condition for the encircling case) as

$$|c_{2,k}| \leq \begin{cases} \sqrt{\frac{3-2e}{4} \left( c_{34,min}^2 - \frac{\epsilon^2}{a^2} \right)} & \text{if } \frac{\epsilon}{a} \leq c_{34,min} < \frac{2-e}{1-e} \frac{\epsilon}{a} \\ \frac{2-e}{2} c_{34,min} - \frac{\epsilon}{2a} & \text{if } c_{34,min} \geq \frac{2-e}{1-e} \frac{\epsilon}{a} \end{cases} \quad (35)$$

The RN separated swarm is designed instead such that all the spacecraft share same phase angles of the  $c_{34}/c_{56}$  vectors, while having these vector separated according to Eq. 30-31. To do so, let design the swarm such that:  $c_{1,k} = 0$ ,  $c_{34,kj} = \|c_{34,k} - c_{34,j}\|_2 \geq c_{34,min} \geq \epsilon/a$ , and  $c_{56,kj} = \|c_{56,k} - c_{56,j}\|_2 \geq c_{56,min} \geq (\epsilon/a)(1+e)$ . Moreover, all the spacecraft must share same phase angles of the  $c_{34}/c_{56}$  vectors,  $\theta_{34}^{sep}$  and  $\theta_{56}^{sep}$ , as:  $\hat{c}_{34,k} \equiv \{ \cos(\theta_{34}^{sep}), \sin(\theta_{34}^{sep}) \}$ , and  $\hat{c}_{56,k} \equiv \{ \cos(\theta_{56}^{sep}), \sin(\theta_{56}^{sep}) \}$ . Given this design, RN PS is enforced for the entire swarm by using Eq. 30-31 evaluated at the perigee (most tight condition) as

$$|\cos(\theta_{34}^{sep} - \theta_{56}^{sep})| \geq \frac{\epsilon(1+e)}{ac_{34,min}c_{56,min}} \sqrt{(c_{34,min})^2 + \left( \frac{c_{56,min}}{1+e} \right)^2} - \frac{\epsilon^2}{a^2} \quad (36)$$

Note that for eccentricity going to zero, these two swarms designs reduce exactly to the ones in [11], with the selected IC state reducing to the quasi-nonsingular ROE through the map in Eq. 38 in Appendix VIII.B. These two

passively-safe spacecraft swarm designs are showcased in the next section, together with a reconfiguration between them enforcing PS in 3-D. This capability is not published in literature and is enabled by Algorithm 1.

## VI. Numerical Results

### A. The Virtual Super Optics Reconfigurable Swarm (VISORS)

Due launch in 2024, VISORS is a two 6U CubeSats distributed telescope that will operate in a near-circular sun-synchronous LEO to image coronal area of the sun with unprecedented resolution [37]. One spacecraft (OSC) contains the optical payload, the other (DSC) contains the detector. During nominal operations, DSC acts as passive chief, whose center of mass sets the RTN frame's origin, whereas OSC actively controls the relative motion. The test cases considered model the challenging "transfer phase", where a passively-safe control plan that moves the formation from the stand-by mode (initial condition) to the science mode (target condition) has to be computed. Both initial and target modes are designed in closed-form to achieve RN PS through relative eccentricity/inclination-separation [6] (Eq. 30-31). Nevertheless, PS has not only to be guaranteed at initial and terminal states, but at every instant of the transfer too. Therefore, Algorithm 1 has to be leveraged to generalize over pure closed-form analysis and compute the transfer. All the parameters of the reconfiguration scenario are reported in Table 2-3. Both a two and five orbits transfers are considered, in which the  $L_2$ -norm of the control input is minimized, and PS is guaranteed in RN plane for at least two orbits ( $T$ ), of at least 3 or 5m ( $\epsilon$ ), at  $3\text{-}\sigma$  confidence ( $q$ ). The uncertainty stems from differential GPS navigation [40], cold-gas impulsive actuation [42] and process-noise modeling the discrepancy between the full-force ground-truth [37, 40] and the on-board dynamics model [19–21]. In particular, looking at Table 2 on the right, the relation between maneuver magnitude and associated actuation execution uncertainty is proportional, which motivates the uncertainty model formalized in Section II. Moreover, looking at Table 3 on the right, the process noise has to account for the unmodeled and possibly stochastic dynamics effects of differential drag present in LEO.

**Table 2 VISORS mission's reconfiguration scenario.**

Reference orbit		Relative orbit modes		Transfer & safety		GPS Navigation [40]		Impulsive Actuation [42]	
Type	Chief	Stand-by ( $t_0$ )	Science ( $t_f$ )	$t_f - t_0$ (orbits)	2 or 5	Uncertainty	1- $\sigma$	Min. Imp. Bit (Ns)	1e-3
$a$ (km)	$R_E + [500 \text{ or } 600]$	$ac_1$ (m)	10 or 0	PS type	RN			Min. Imp. Incr. (Ns)	6e-5
$e$ (-)	0.001	$ac_2$ (m)	-100	$T$ (orbits)	2	Abs. Position. (m)	1	Uncertainty	1- $\sigma$
$i$ (deg)	98	$ac_3$ (m)	0	$\epsilon$ (m)	3 or 5	Abs. Velocity (cm/s)	1	Maneuver Magn. (%)	5
$\Omega$ (deg)	252 or 330	$ac_4$ (m)	200	$q$ ( $\sigma$ )	3	Rel. Position (cm)	1	Maneuver Dir. (arcmin)	1
$\omega$ (deg)	0 or 45	$ac_5$ (m)	0	$\mathcal{J}$ (m/s)	$\sum_{ki} \ \bar{a}_k(t_i)\ _2$	Rel. velocity ( $\mu\text{m/s}$ )	25		
$\nu(t_0)$ (deg)	-90 or 1	$ac_6$ (m)	200	$n_M$ (-)	25 or 75				
Period (h)	1.58			$n$ (-)	720 or 1800				
Epoch	1-1-2024			$m$ (-)	720 or 720				
GPS time	00 <sup>h</sup> :00 <sup>m</sup> :00 <sup>s</sup>								

**Table 3 Spacecraft features and dynamics models.**

Spacecraft features		Dynamics models			
Mass (kg)	12	Geopotential	Ground-truth [37, 40]	On-board prediction [37]	On-board optimization [19–21]
Cross-section area ( $m^2$ )	nom: 0.285	Atmospheric drag	GGM01S ( $60 \times 60$ ) [43]	GGM01S ( $20 \times 20$ ) [43]	$J_2$ secular & long-period
	avg: 0.206		NRLMSISE00 [44]	NRLMSISE00 [44] (with constant 1000% error)	Secular & long-period model-free
$C_d$ (-)	2.3	Solar radiation pressure	Cannonball model, no eclipses	None	Secular & long-period proportional to differential ballistic coefficients
$C_r$ (-)	1.88	Third-body gravity	Analytical lunisolar ephemerides	None	Luni-solar secular & long-period
		Integrator	RK4	RK4	Euler
		Step size	Fixed: 30s	Fixed: 60s	Fixed: see Table 2
		Process-noise on IC (m/orbit)	None	None	3

#### 1. Two-orbits Transfer

Algorithm 1 is used to solve for the two orbits transfer. The solution of the convex two-point-boundary-value-problem (TPBVP) [39] is used as initial warm-start,  $MAX\_ITER$  is set to 3, and trust-regions varying from 100m to 5m along the transfer are implemented. The underlying optimization problem is a second order cone program (SOCP) [38]. The

optimizer looks for candidate impulsive maneuvers every 30deg along the orbit, so  $n_M = 25$ , whereas the discretization at which PS must be enforced is at 1deg, therefore  $n = m = 720$ . PS is enforced after each maneuver application to guarantee safety both on the trajectory in between maneuvers and, in case of subsequent maneuver failure, afterwards up to  $t_f + T$ . Given the selected orbit discretization, the proposed efficient  $\mathcal{M}^*$ -formulation permits to reduce the number of constraints required to enforce PS from  $> 25 \times 720 = 18000$  to 25. By explicitly enforcing these constraint within the SOCP, this implies in average a computational saving of a factor  $> 100$  (from  $\sim 33s$  to  $\sim 0.27s^{\ddagger}$ ) on the solution of an instance of Problem III.2 using a SOCP solver [39]. The computational overhead introduced by the precomputation of  $t_{k_jil}^*$  is minimal, since it is performed jointly with the precomputations required to evaluate  $\beta_{k_jil}$  as well as other matrices needed in the SOCP, for a total execution time of  $\sim 1s$ . Note that, if all the thousands constraints are enforced explicitly and  $t_{k_jil}^*$  is not computed, precomputations are still needed at each SCP iteration but may be slightly lighter (depending on the implementation). On the other hand, the computational gain obtained on the solution of the SOCP by enforcing just 25 constraints is much greater. Figure 7 enlarges this analysis showing the results of a Monte Carlo on

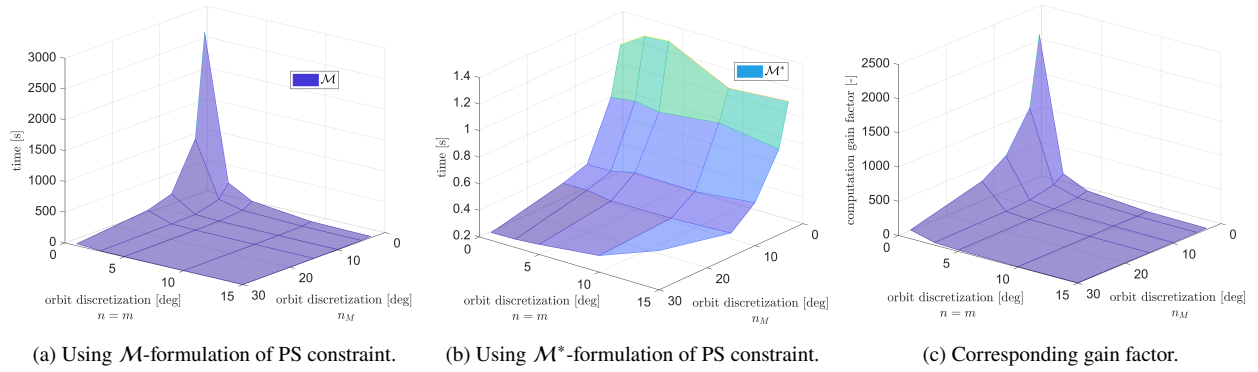


**Fig. 7** Monte Carlo analysis on the computational effort of solving a SOCP instance, by varying the orbit discretization between maneuvers ( $n_M$ ) and at which safe separation must be enforced ( $n = m$ ).<sup>‡</sup>

the computational effort by varying the selected orbit discretization. Looking at Figures 7a-7b, the expected correlation between time/orbit discretization, number of constraints, and computation time is clear. In particular, the computational effort trends using the  $\mathcal{M}$  and  $\mathcal{M}^*$ -formulations follow closely the ones of the number of enforced constraints presented in Figure 2. Looking at Figure 7c, the resulting computational saving factor depends on the time/orbit discretization, and it is up to 3 orders of magnitudes. This validates the benefit of the proposed  $\mathcal{M}^*$ -formulation of the PS constraint.

In Figure 8, the resulting optimal transfer trajectory of the OSC around the DSC (at the origin) is presented both in 3-D RTN space and projected in 2-D RN plane. In particular, the controlled motion (blue bold line) is always instantaneously tangent to a safe uncontrolled trajectory (dashed lines), which is followed if the OSC loses control at that instant. Spacecraft separation along the uncontrolled trajectories is guaranteed to be  $\geq 3m$  for at least 2 orbits, accounting for  $3-\sigma$  uncertainty (blue shaded ellipsoids). This is achieved in closed-loop. In particular, the black dot-dashed "closed-loop plan" line is the trajectory planned on-board. The blue "controlled true" line is obtained by executing the control plan through actuation and propagating the resulting motion through the ground-truth dynamics. The difference between these two lines lies in the difference between the on-board dynamics model used for optimization and the ground-truth, as well as in the errors introduced by navigation and actuation. Similar can be said for the dashed "uncontrolled" trajectories. The blue ones are obtained integrating the ground-truth dynamics after each possible contingency. The black ones are predicted on-board and have superimposed the  $3-\sigma$  ellipsoids modeling the uncertainty distributions used to compute the bounds  $\beta_{k_jil}$ . The true uncontrolled trajectories are contained within the  $3-\sigma$  ellipsoids implying that the uncertainty distributions rightly capture and compensate for the difference between on-board belief and reality. Note how larger uncertainty manifests after larger maneuvers application, due to the correlation between maneuver magnitude and actuation uncertainty presented in Table 2 on the right. Comparing the control profile in Figure 9a and the uncertainty ellipsoids in Figure 8, after the largest planned maneuver (second one), the generating uncontrolled trajectory is characterized by very large uncertainty that has to be kept out of the origin in RN plane to have PS guarantees. This causes the algorithm to allocate a large bound ( $\beta_{k_jil}$ ) on the minimum separation to be kept

<sup>‡</sup>Computation times reported are from a Windows system equipped with a 4GHz processor and 64GB RAM.

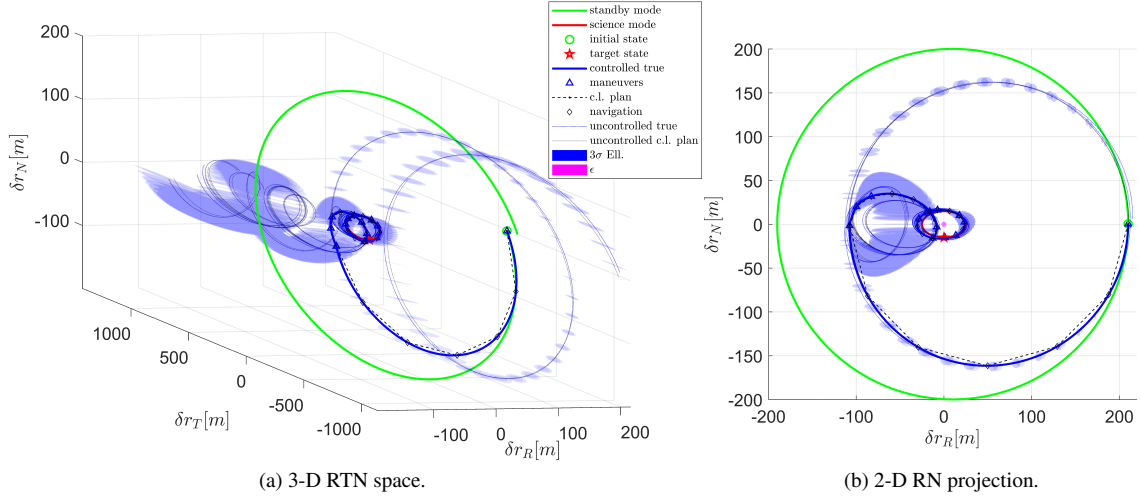


**Fig. 8 Two-orbits passively-safe transfer trajectory.**

on the generating uncontrolled trajectory. The varying size of such quantified bound in relation to the size of the applied maneuvers can be appreciated by comparing the pink ( $\epsilon + \beta_{kjil}$ ) dashed lines in Figure 9c, with the control profile. The

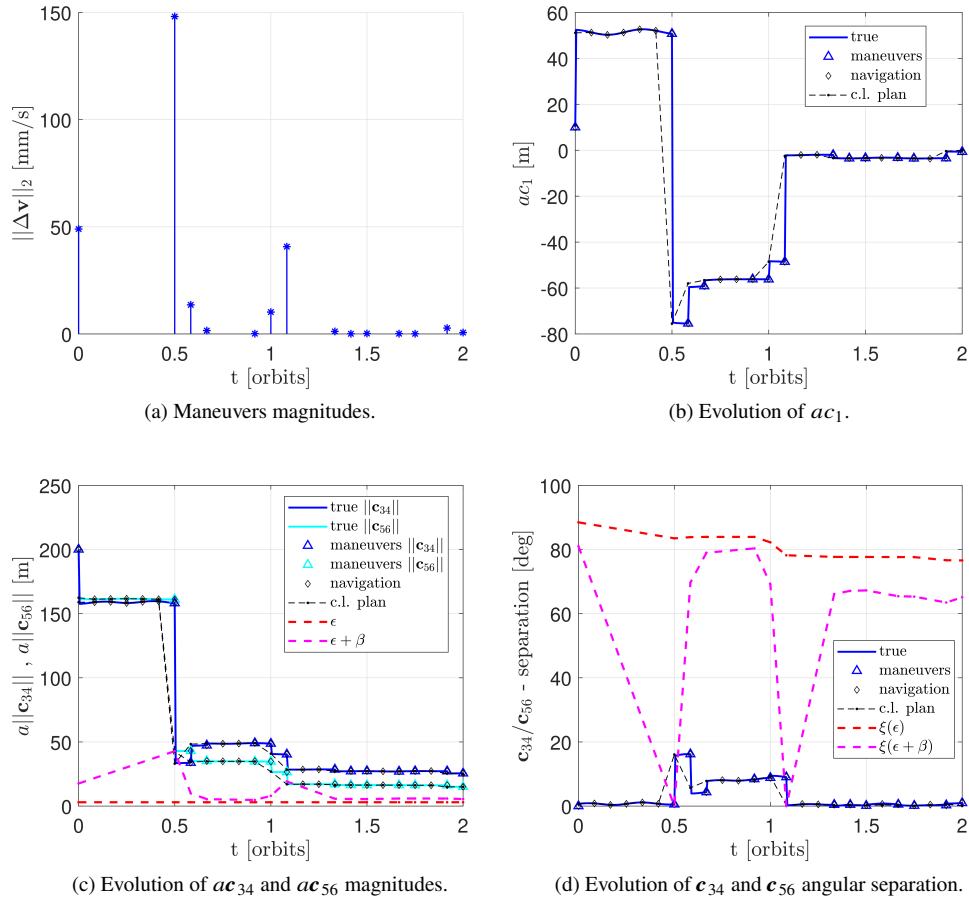


**Fig. 9 Maneuver magnitudes profile and IC trajectories over the two-orbit transfer.**

total control cost of the transfer is 0.27m/s. The cost of the TPBVP is  $\sim 0.253$ m/s. A difference of 10%, considering the included constraints and uncertainties, represents a very fuel efficient transfer, well within the  $\sim 0.3$ m/s allocated in the mission delta-V budget [37].

Finally, to compare with the closed-form analysis presented in Section V.A, Figure 9 shows the evolution over the transfer of  $ac_1$ , the magnitude of the vectors  $ac_{34}/ac_{56}$ , and their angular separation. The magnitude of  $c_{34}$  and  $c_{56}$  sizes the ellipses drawn by uncontrolled trajectories in RN plane (see Figure 5, right), their angular separation relates to PS through Eq. 30, whereas,  $c_1$  represents an off-set in radial direction of these ellipses (see Eq. 37, in Appendix VIII.B). The trajectory computed using direct optimization achieves PS in RN plane either by having these ellipses centered around the origin with size  $\geq \epsilon + \beta_{kjil}$ , or, by decentering them in radial direction through a sufficiently large  $|c_1|$  if their size is  $< \epsilon + \beta_{kjil}$  (see Figure 8b). This analysis is validated in Figure 9. At the second maneuver, the reduction of the  $c_{34}$  and  $c_{56}$  norms requires  $c_1 \approx -80$ m to achieve PS in RN plane. Comparing Figures 9c and 9d, when the norm of  $c_{34}$  or  $c_{56}$  becomes  $< \epsilon + \beta_{kjil}$ ,  $\xi_{kjil}$  (Eq. 30) shrinks so much that safe separation is not possible by centering the RN ellipse around the origin. Therefore PS is achieved by properly decentering the ellipse in radial direction. The notable aspect is that such clear geometrical insight and deep connection with closed-form analysis is obtained using Algorithm 1 and underlying convex optimization. This opens the way to much greater generalization and applicability reach than the specialized closed-form solutions.

## 2. Five-Orbits Transfer

The five orbits transfer reflects more closely what it is envisioned for the real mission. Differently from the two orbit one, where the TPBVP solution was used as initial warm-start, now an initial open-loop design is made such as to achieve RN PS throughout the transfer using closed-form analysis under simplifying assumptions on the dynamics and neglecting system uncertainties [36, 37]. Table 4 presents the statistics of a Monte Carlo of 25 transfers realized by

**Table 4 Comparison between approaches. Monte Carlo analysis over 25 transfers.**

	Terminal state errors							Other metrics				
		$\epsilon_{c_1}$ (m)	$\epsilon_{c_2}$ (m)	$\epsilon_{c_3}$ (m)	$\epsilon_{c_4}$ (m)	$\epsilon_{c_5}$ (m)	$\epsilon_{c_6}$ (m)	$\mathcal{J}$ (m/s)	$\min(S^{*RN})$ (m)	time <sup>‡</sup> (s)	# calls (-)	PS Guarantees
Open-loop design [36, 37]	mean	4.40	164.89	1.63	3.86	1.33	5.44	0.324	15.91	0.71	1	Enforced
	std	3.01	110.25	0.88	2.99	0.73	3.91	0	3.42	0.24	-	in open-loop
Algorithm 1 + Tracking (Sec. IV.B [36])	mean	0.07	1.84	0.13	0.21	0.16	0.16	0.264	16.69	Alg. 1: 3.48 Track. : 1.48	5 75	Enforced
	std	0.06	1.88	0.17	0.12	0.20	0.11	0.004	0.37	Alg. 1: 0.33 Track. : 0.08	1 -	in closed-loop
Closed-form tracking [45]	mean	0.46	6.35	0.49	1.30	0.62	1.09	0.333	16.70	0.0032	3	Checked
	std	0.32	4.73	0.55	0.95	0.63	0.90	0.01	0.91	0.0030	-	a posteriori

implementing the control profiles within the ground-truth dynamics accounting for actuation errors and in presence of the various uncertainty sources introduced in Table 2-3. Looking at the top, when implemented in the ground-truth, the open-loop control design does not reach the desired terminal state (errors in along-track  $> 100$ m). Therefore, to retrieve closed-loop properties tracking is needed. This is done in two different ways. The first, Table 4 on the bottom, uses state-of-the-art closed-form impulsive control solutions [45]. The second, Table 4 on the center, feeds the open-loop plan as initial warm-start to Algorithm 1 which refines it, and then tracks it using the logic presented in Section IV.B. These two approaches are compared in the following. The transfer trajectory obtained using Algorithm 1 + tracker is shown in Figure 10. The controlled motion (blue bold line) is always instantaneously tangent to a safe uncontrolled trajectory (dashed lines), which is followed if the spacecraft loses control at that instant. Spacecraft separation along the uncontrolled trajectories is guaranteed to be  $\geq 5$ m for at least 2 orbits, accounting for 3- $\sigma$  uncertainty (blue shaded ellipsoids). The level of uncertainty in the five orbits transfer is lower than in the two orbits one due to the smaller applied maneuvers, and consequently smaller actuation uncertainty. More extensive results are in [36].

The closed-form tracker [45] computes a correction to the open-loop control profile every 1.5 orbits to null the expected terminal state error. The correction is a maneuver sequence composed by three tangential and two normal maneuvers. Looking at Table 4 on the bottom, good performances in terms of average terminal state error and PS ( $\min(S^{*RN})$ ) are retrieved, at a very small average computational cost ( $< 0.005$ s, for computing the correction over the subsequent 1.5 orbits). The benefits of this approach are the simplicity, the explainability and computational efficiency. The main limit is that formal guarantees of PS are not provided. In particular, the closed-form tracker achieves PS by

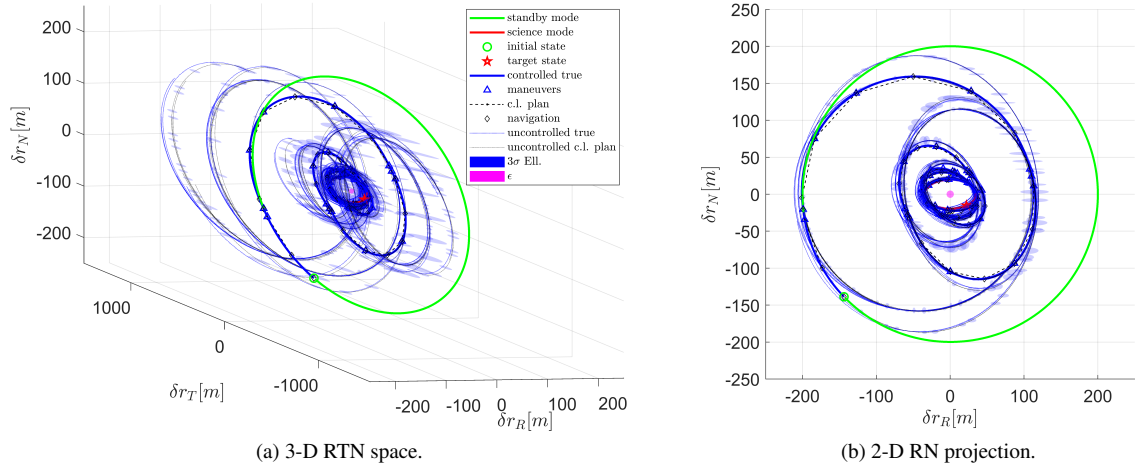


**Fig. 10** Five-orbits passively-safe transfer trajectory.

tracking closely the open-loop trajectory, designed to satisfy RN PS. The closed-loop trajectory results a posteriori to be passively-safe, but no explicit constraints are enforced during the closed-loop plan computation. In order to employ this algorithmic solution on-board it must be complemented with an additional logic that checks after each maneuver application the PS margin and, if needed, computes an escape maneuver if the safety limit is violated. Moreover, since the closed-loop tracker looks for correction maneuvers on-top of the open-loop plan, it achieves a total control cost which is  $\geq$  than the open-loop one.

As presented throughout this paper, Algorithm 1 instead looks for hard guarantees of PS. Using the open-loop design as warm-start, Algorithm 1 looks for candidate maneuvers every 30deg plus in the locations of the open-loop design ones, for a total of  $n_M = 75$  maneuver candidates over  $[t_0, t_f]$ . As done for the two orbits transfer, PS is enforced after each maneuver application to guarantee safety both on the trajectory in between maneuvers and, in case of subsequent maneuver failure, afterwards up to  $t_f + T$ . The time discretization at which PS must be enforced is at 1deg so 1800 samples on  $[t_0, t_f]$  and 720 samples on  $(t_f, t_f + T]$ . The proposed efficient  $\mathcal{M}^*$ -formulation permits to reduce the number of constraints required to enforce PS from  $> 75 \times 720 = 54000$  to 75. The benefit from a computational standpoint is analogous to the one presented for the two orbits transfer. Looking at Table 4 in the middle, Algorithm 1 achieves an average terminal state error  $\sim 80\%$  smaller, and a total delta-V  $\sim 20\%$  smaller, than the closed-form tracker. This is mainly due to the refinement of the initial warm-start over a larger optimization search space of maneuver candidates. In general, the benefits introduced by Algorithm 1 are the hard safety guarantees, high control accuracy performances, and flexibility of optimizing over a larger design space leading to a more fuel-efficient solution. The main limits are the lower explainability with respect to the closed-form solutions and the increased average computational cost. Looking at the run times presented in Table 4, using Algorithm 1 takes in average  $\sim 3.5s$ , whereas the tracker (Section IV.B [36]) takes in average  $\sim 1.5s$ . Note that the run time depends on various SCP parameters and tolerances which can be tuned to trade with other performance parameters, as the fuel optimality reached at convergence. The ratio of Algorithm 1 and tracking calls over the transfer is dictated by the high-level logic presented at the end of Section IV.B. Specifically, over the 75 decision points, Algorithm 1 is used once at the beginning and then other 4 times, of which 100% of them are due to tracking unfeasibility. This shows that the main trigger in recomputing the "guidance" plan is the incapability to remain within the specified tracking bounds, and not much having the predicted worst-case minimum RN separation lower than  $\epsilon$ , which would entail a much greater risk from a safety perspective. Given the computational constraints for on-board implementation on the CubeSats microprocessors and looking at the average computational cost of using Algorithm 1 with respect to the tracking, ideal would be to use Algorithm 1 just once at the beginning of the transfer and then track. In this sense parameters as the specified size of the tracking bound ( $v_{ki}^T$ ) can be properly tuned to prevent unnecessary re-plannings and reduce the overall computational expense.

## B. Spacecraft Swarm in Eccentric Orbits

In this section, Algorithm 1 is assessed on the centralized open-loop trajectory design of a spacecraft swarm reconfiguration test case in highly eccentric orbit (HEO) around Earth. Three spacecraft have to reconfigure with respect to a virtual reference. The initial and target conditions are correspondingly an "high-density" (Eq. 35) and an RN separated (Eq. 36) swarm designs as defined in Section V.B. Such conditions are depicted graphically in Figure 11 in IC space, and in Figures 12a and 12c in Cartesian RTN space, and further characterized in Table 5. Figures 12b and 12d show the spacecraft separations over the initial and target relative orbits. It is clear how the initial swarm configuration is safely separated in RT plane but not in RN, and the target one, viceversa, is safely separated in RN plane but not in RT.

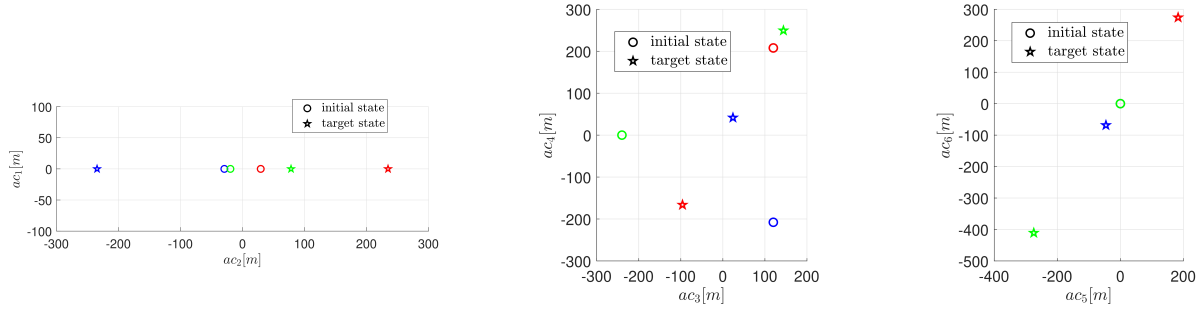


**Fig. 11 Initial RT-separated and target RN-separated swarm designs in IC space.**

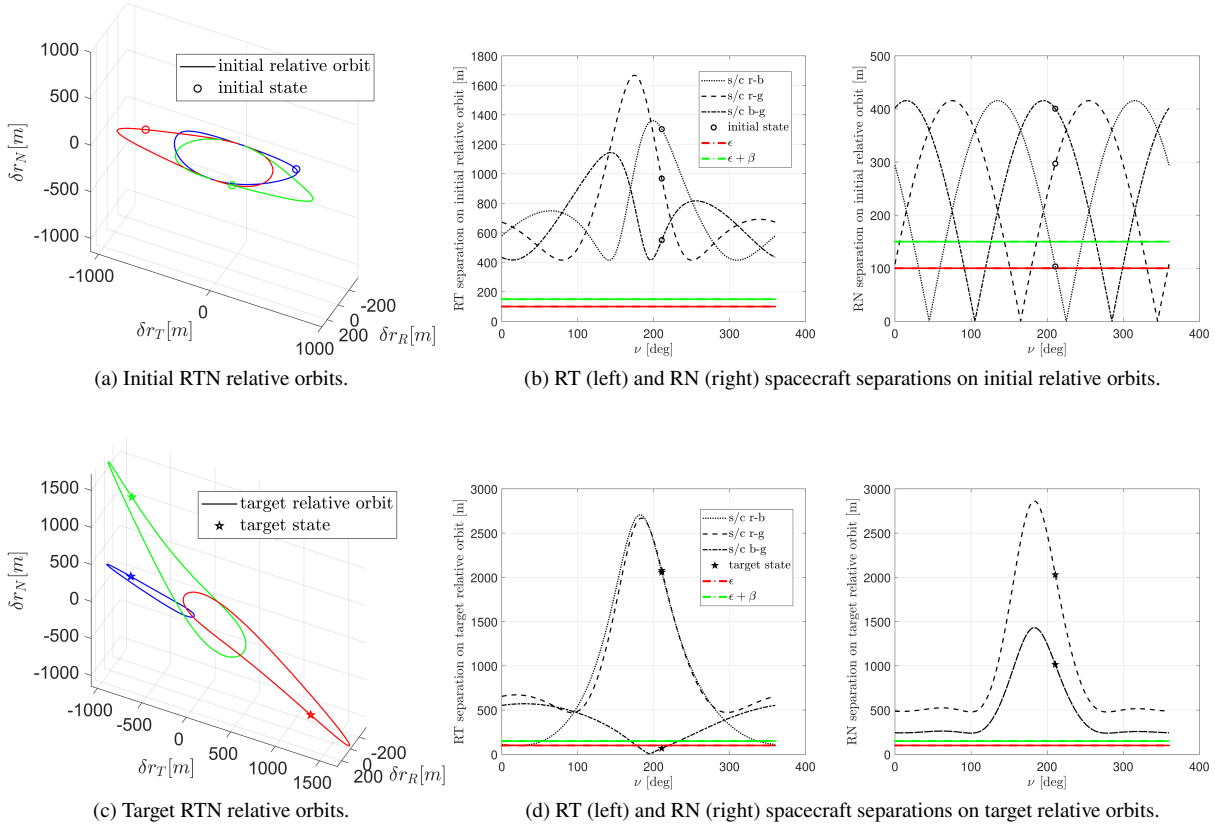


**Fig. 12 Swarm initial and target relative orbits, and corresponding separation trends.**

A reconfiguration between the two designs while enforcing PS in 3-D is showcased, demonstrating a capability not published in literature. The reconfiguration horizon is fixed to two reference orbit periods, and PS has to be guaranteed in 3-D for at least one orbit ( $T$ ), of at least 100m ( $\epsilon$ ). This open-loop trajectory design is treated as deterministic, therefore

**Table 5 Highly eccentric orbit (HEO) Swarm Test Case.**

Reference orbit		Relative orbit modes		Transfer & safety		Spacecraft & features		
Type	Virtual		Initial ( $t_0$ )	Target ( $t_f$ )	$t_f - t_0$ (orbits)	2	Mass (kg)	80
$a$ (km)	24641	$ac_1$ (m)	[0,0,0]	[0,0,0]	PS type	3-D	Cross Sec. Area (m <sup>2</sup> )	0.4
$e$ (-)	0.716	$ac_2$ (m)	[29.3,-29.3,-19.6]	[234.6,-234.6,78.2]	$T$ (orbits)	1	$C_r$ (-)	1.88
$i$ (deg)	7	$ac_3$ (m)	[120.0,120.0,-240.0]	[-96.0,24.0,144.0]	$\epsilon$ (m)	100	Thrust (mN)	50
$\Omega$ (deg)	-10	$ac_4$ (m)	[207.9,-207.9,0]	[-166.3,41.6,249.4]	$\beta$ (m)	50	$\zeta_i$ (m/s)	$\frac{\text{Thrust}}{\text{Mass}} \Delta t_i$
$\omega$ (deg)	135	$ac_5$ (m)	[0,0,0]	[183.1,-45.8,-274.6]	$n$ (-)	24		
$\nu(t_0)$ (deg)	210.6	$ac_6$ (m)	[0,0,0]	[273.9,-68.5,-410.9]	$m$ (-)	12		
Period (h)	10.7	$ac_{34,min}$ (m)	240	240	$N_a$ (-)	3		
Epoch	1-1-2021	$ac_{56,min}$ (m)	-	411.8	$\mathcal{J}$ (m/s)	$\sum_{k_i} \ \ddot{\mathbf{u}}_k(t_i)\ _2$		
GPS time	00 <sup>h</sup> :00 <sup>m</sup> :00 <sup>s</sup>	$\theta_{34}^{hd}$ (deg)	120	-				
		$\theta_{34}^{sep}$ (deg)	-	60				
		$\theta_{56}^{sep}$ (deg)	-	236.2				

no uncertainty sources are included. The spacecraft relative motion dynamics is modeled as Keplerian perturbed by Earth oblateness ( $J_2$ ) and solar radiation pressure (SRP) [21]. Being the considered scenario deterministic, the only contribution to be accounted in the quantification of the bound  $\beta_{k,jil}$  in Eq. 19 is the integrated effect of  $J_2$ +SRP over the PS horizon. Moreover, while in presence of uncertainties the quantification of such bound must be corrected in closed-loop within Algorithm 1, when just deterministic effects are included, the worst case expected effect of non-integrable dynamics over the PS horizon can be quantified a priori. This is done for this test case, and a constant PS bound ( $\beta = 50\text{m}$ ) is considered. The spacecraft are modeled as continuously controlled by low-thrust actuation. To mimic the realizability of the control profile by the considered actuation a cap  $\zeta$  on the control input  $L_2$ -norm is imposed. In particular, given a constant thrust and the spacecraft mass, using second Newton law,  $\zeta_i = (\text{Thrust}/\text{Mass})\Delta t_i$ , where  $\Delta t_i$  is the maximum interval over which a computed delta-V must be realized by the low-thrust. This implies a convex constraint on the control input. The  $L_2$ -norm of the control input is minimized. The orbit is discretized at 30deg, entailing a time-variant time step ( $\Delta t_i$ ) given the spacecraft varying velocity along the eccentric orbits.

### 1. Results

For this test case, a comparison between PS and standard collision avoidance (CA) is presented. In particular, when enforcing CA, the horizon is  $T = 0$  by definition. All the subroutines in Algorithm 1 related to the computation of  $t_{k,jil}^*$  disappear, and the constraint is simply linearized in the SCP as done in literature [24, 25, 30]. To warm-start the CA SCP solver the convex TPBVP solution [39] is used. When enforcing PS instead, a safety horizon  $T = 1$  orbit is considered, and the solution enforcing CA is used as first attempt of warm-start. The results of the comparison are reported in Figure 13 and in Table 6. In particular, looking at Figure 13b, if CA is enforced, when red-spacecraft loses control (red asterisk) the resulting uncontrolled trajectory (red dashed line) reaches a minimum separation of  $57.6\text{m} < \epsilon$  with respect to the uncontrolled trajectory of blue-spacecraft (blue dashed line) originated from a previous contingency (blue asterisk). Looking at Figure 13a, if PS is enforced, the same contingencies result in uncontrolled trajectories that maintain safe separation. Looking at Figures 13c and 13d, this analysis is expanded to all the possible combinations of contingencies and corresponding separations on the time span  $[t_0, t_f + T]$  equal to 3 orbits. The black line is  $\mathcal{S}_{k,jil}^*$  which assumes integrable dynamics on the uncontrolled arcs, the purple line accounts for  $J_2$ +SRP effects. In Figure 13c,  $\mathcal{S}_{k,jil}^*$  is enforced being  $\geq \epsilon + \beta$ , and the worst case effect of perturbations is lower than  $\beta$ , this provides guarantee of PS. In Figure 13d, both black and purple lines go lower than  $\epsilon$  violating the PS constraint. This comparison is summarized in Table 6 on the right. Both CA and PS guarantee a minimum separation  $\geq \epsilon$  when no contingencies happen. Accounting for contingencies instead, PS guarantees the separation on the uncontrolled trajectories being greater than  $\epsilon$ , whereas CA does not. Looking at the control costs in Table 6 on the left, the number reported are totals for the entire swarm. The control cost of the solution enforcing PS is 2% larger than the one enforcing CA. This is a fuel efficient solution considering the additional number of constraints included. Looking at the run times in Table 6 on the center, enforcing PS is more computational expensive than enforcing CA. This larger computational expense is related to two factors. Firstly, the number of constraints to be enforced in each underlying SOCP, which is larger for PS ( $n^2 N_a(N_a - 1)/2$ ) than for CA ( $n N_a(N_a - 1)/2$ ). Secondly, the computations in Algorithm 1 (lines 9-24) required for convergence to a passively-safe solution given an initial warm-start that is not necessarily feasible (e.g., that satisfies CA but not PS). The convergence trend is the one presented in Figure 4b. In particular, the farthest is the initial warm-start from being feasible, the more inner-loop iterations are needed to converge, the more solutions of SOCP instances [39]

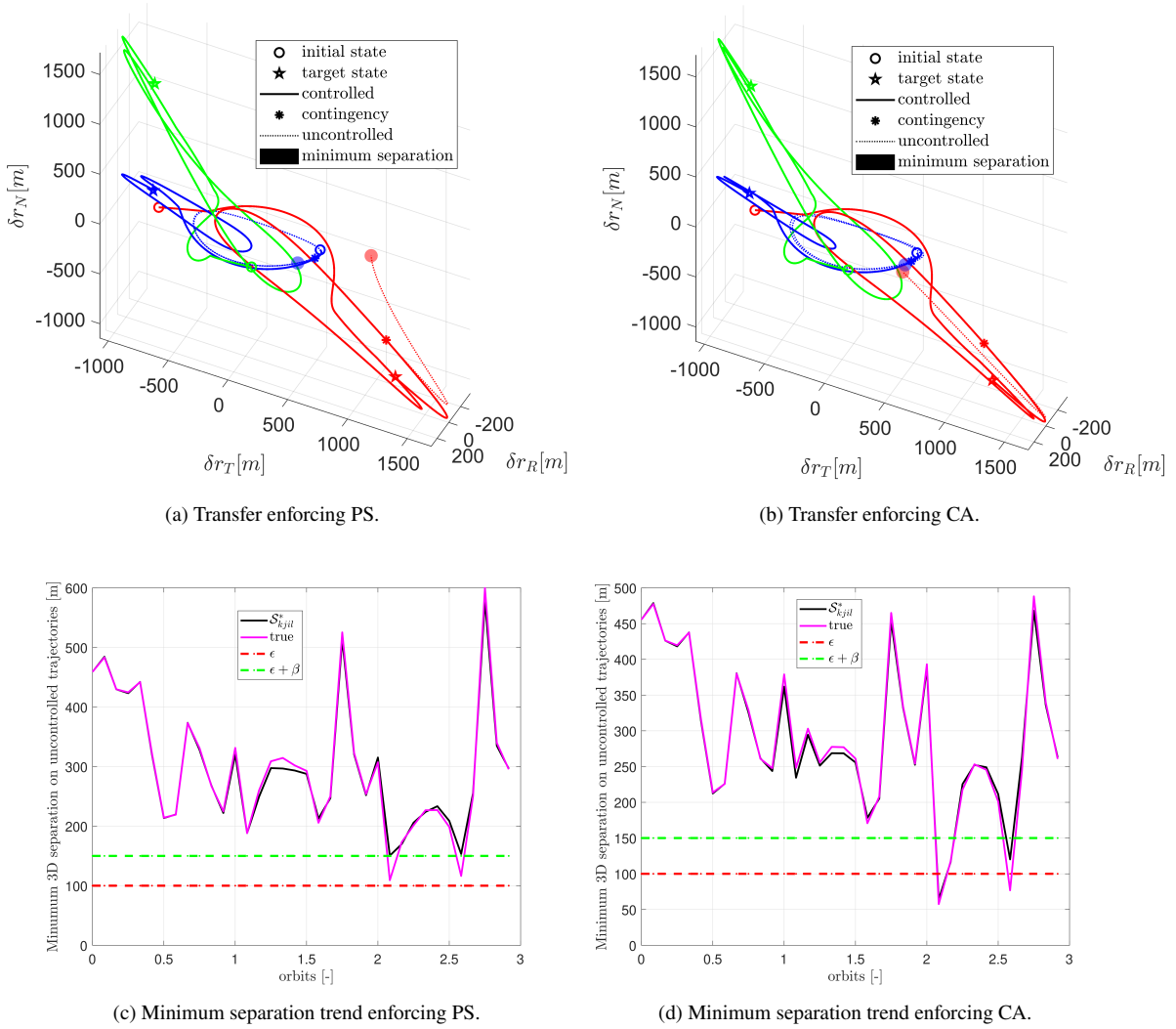


**Fig. 13** Optimal transfer trajectories and corresponding swarm's minimum separations up to  $t_f + T$  accounting for all possible combinations of contingencies on  $[t_0, t_f]$ .

**Table 6** Comparison of PS and standard collision avoidance (CA).

Control cost	# Constraints	Running time <sup>‡</sup>		$\epsilon$	$\min_{k,j,l} S_{k,j,l}^*$	
		Warm-start			No contingencies	With contingencies
(m/s)	(-)	(-)	(s)	(m)	(m)	(m)
PS	$n^2 \frac{N_a(N_a-1)}{2}$	CA	34.5	100	188.2	109.2
		PS	6.3			
CA	$n \frac{N_a(N_a-1)}{2}$	TPBVP	2.8	100	248.3	57.6 ( $< \epsilon$ )

including  $n^2 N_a(N_a - 1)/2$  constraints are required, the higher the overall computational cost. Consequently, a bad initial warm-start has a substantial impact. Looking at Table 6, this is further proved by feeding-back as warm-start a previously found passively-safe solution. Now, Algorithm 1 is  $\sim 5$  times faster in converging to a fuel efficient transfer. This test case underlines the importance of properly warm-starting SCP-based algorithms to cut their computational expense, in particular for on-board execution.

## VII. Conclusion

Fault-tolerant motion safety strategies are important in risk-adverse and failure-sensitive applications as miniaturized distributed space systems (DSS), employing low-size-weight-and-power as well as commercial-of-the-shelf components. Different strategies are possible, this paper focuses specifically on multi-agent passive safety (PS), which consists in providing guarantees of safe separation even in case of sudden loss of control capabilities by any agent, while in presence of system uncertainties. This paper formalizes a mathematical approach based on variation of parameters that permits to model efficiently dynamics dependent constraints with application to fault-tolerant control. This is used to enforce efficiently PS within an multi-agent optimal control problem solvable through direct methods. Moreover, the paper shows how a control profile enforcing PS in closed-loop in a multi-agent setting can be obtained through an algorithm based on sequential convex programming (SCP) and model predictive control. This is used to achieve passively-safe DSS reconfigurations in scenarios out of the assumption limits of the current literature, both in near-circular and eccentric orbits, in presence of realistic system uncertainties from sensing, actuation, and unmodeled system dynamics. In addition, the application of the proposed mathematical approach to the DSS dynamics permits to derive novel solutions for multi-spacecraft PS in eccentric orbits, with relevant applications to relative motion design and guidance.

The directions of future research are multiple. Firstly, the generality of the proposed mathematical approach opens the door to new applications, both in terms of different constraints and in terms of different multi-agent systems, for which efficient fault-tolerant guarantees are relevant. Secondly, there is surely interest in extending the proposed framework to contingencies that do not entail complete loss of control capabilities (e.g., degradations). In the DSS application, these could model relevant scenarios such as leakages, stuck-off thrusters, and others. A first solution, directly within the framework presented in this paper, is to model the residual degraded control as additional process noise within the formalized uncertainty model, which can be even upgraded to account for non-Gaussian effects (e.g., using Gaussian mixtures or unscented transforms). Thirdly, looking at the on-board implementation, the role of warm-starts to speed up the SCP-based solvers is key, as it is important exploring the role of discretization in continuous control while including failures modes, and studying feasibility guarantees given an arbitrary set of initial conditions and optimization parameters. The vision is that the framework presented in this paper, complemented with informed warm-starts, decentralization of the computations, and proactive/reactive approaches to be triggered upon unfeasibility in finding a passively-safe solution, can enable safe and fault-tolerant real-time motion planning and control on-board, which is the core requirement for autonomous functions in future DSS missions.

## VIII. Appendix

### A. Passive Safety Constraint Requirements

In the following, formal proof of the number of constraints required to enforce PS reported in Table 1 is developed. The proof is developed for the "impulsive" control type, it is left to the reader verifying that for  $n_M \rightarrow n$ , the number of constraints required in impulsive control tends to the ones required in continuous control. The number of active agents' combinations is  $N_a(N_a - 1)/2$ , where  $N_a$  is the number of active agents.  $N_p$  is the number of permanently passive agents.

**Proposition VIII.1.** *Assuming the interval  $[t_0, t_f]$  is discretized in  $n$  samples, and the interval  $(t_f, t_f + T]$  in  $m$  samples. Assuming impulses are applied and possibly failed just in a subset  $n_M \leq n$  of the  $n$  instants, such as  $n/n_M \in \mathbb{N}_{>0}$ . In order to guarantee PS (as in Definition III.1) at each of the  $n$  and  $m$  instants in  $[t_0, t_f + T]$ , using the  $\mathcal{M}$ -formulation, the total number of collision avoidance constraints the multi-agent system has to enforce is:  $[(n/n_M)(\sum_{i=1}^{n_M} i^2) + (n_M + 1)^2 m]N_a(N_a - 1)/2 = \{(n/n_M)[n_M(n_M + 1)(2n_M + 1)/6] + (n_M + 1)^2 m\}N_a(N_a - 1)/2$ , with order of magnitude:  $O((n + m)n_M^2 N_a^2)$ . Whereas, between active and permanently passive agents is:  $[(n/n_M)(\sum_{i=1}^{n_M} i) + (n_M + 1)m]N_a N_p = \{(n/n_M)[n_M(n_M + 1)/2] + (n_M + 1)m\}N_a N_p$ , with order of magnitude:  $O((n + m)n_M N_a N_p)$ . Using the  $\mathcal{M}^*$ -formulation, the total number of IC-dependent functions to be constrained between active agents is:  $n_M^2 N_a(N_a - 1)/2$ . Whereas, between active and permanently passive agents is:  $n_M N_a N_p$ .*

*Proof.* Looking at Figure 1b, in between each of the instants  $t_i \in [t_0, t_f]$ ,  $i = 1, \dots, n_M$ , of impulsive control application, the number of separations' combinations to be constrained is  $(n/n_M)i^2 N_a(N_a - 1)/2$  between active agents, and  $(n/n_M)i N_a N_p$  between active and permanently passive agents. Where the factor  $(n/n_M)$  accounts for the need of guaranteeing safe separation in-between the impulses, too. Instead on  $(t_f, t_f + T]$ , at each of the  $m$  instants, the number of separation combinations to be constrained is  $(n_M + 1)^2 N_a(N_a - 1)/2$  between active agents, and  $(n_M + 1)N_a N_p$  between active and permanently passive ones. The +1 in the  $n_M + 1$  factor accounts for the case in

which control is not lost on  $[t_0, t_f]$ , but the reached target configuration has to be guaranteed safe with respect to the uncontrolled trajectory of another agent. This implies that the total number of separation combinations to be constrained over  $[t_0, t_f + T]$  to have guarantee of PS between active agents is:  $[(n/n_M)(\sum_{i=1}^{n_M} i^2) + (n_M + 1)^2 m] N_a (N_a - 1)/2$ , with order of magnitude:  $O((n+m)n_M^2 N_a^2)$ . Whereas, between active active and permanently passive agents is:  $[(n/n_M)(\sum_{i=1}^{n_M} i) + (n_M + 1)m] N_a N_p$ , with order of magnitude:  $O((n+m)n_M N_a N_p)$ . The total number of IC-dependent functions to be constrained equates the total number of IC states' combinations involved in Eq. 17. Which, as highlighted in Remark II.2, equates the number of contingency instants' combinations. Therefore, to enforce PS between active agents, the total number of IC states' combinations to be constrained is:  $n_M^2 N_a (N_a - 1)/2$ . Whereas, between active active and permanently passive agents is:  $n_M N_a N_p$ . Which concludes the proof.  $\square$

## B. Relative Motion Dynamics

The fundamental matrix solution of the linear(ized) integrable part of Eq. 27 is

$$\Psi(t) = a \begin{bmatrix} \frac{1}{\rho} - \frac{3}{2} \frac{e}{\eta^3} \sin(\nu) nt & 0 & -\cos(\lambda_\nu) & -\sin(\lambda_\nu) & 0 & 0 \\ -\frac{3}{2} \frac{\rho}{\eta^3} nt & \frac{1}{\rho} & (\frac{1}{\rho} + 1) \sin(\lambda_\nu) & -(\frac{1}{\rho} + 1) \cos(\lambda_\nu) & 0 & 0 \\ 0 & 0 & 0 & 0 & \frac{1}{\rho} \sin(\lambda_\nu) & -\frac{1}{\rho} \cos(\lambda_\nu) \\ -\frac{1}{\rho^2} \dot{\rho} - \frac{3}{2} \frac{e}{\eta^3} \cos(\nu) \dot{\nu} nt & 0 & \sin(\lambda_\nu) \dot{\nu} & -\cos(\lambda_\nu) \dot{\nu} & 0 & 0 \\ -\frac{3}{2} \frac{e}{\eta^3} \sin(\nu) n & 0 & -\frac{1}{\rho^2} \dot{\rho} \sin(\lambda_\nu) & \frac{1}{\rho^2} \dot{\rho} \cos(\lambda_\nu) & 0 & 0 \\ -\frac{3}{2} \frac{\dot{\rho}}{\eta^3} nt - \frac{3}{2} \frac{\rho}{\eta^3} n & -\frac{1}{\rho^2} \dot{\rho} & +(\frac{1}{\rho} + 1) \cos(\lambda_\nu) \dot{\nu} & +(\frac{1}{\rho} + 1) \sin(\lambda_\nu) \dot{\nu} & 0 & 0 \\ 0 & 0 & 0 & 0 & -\frac{1}{\rho^2} \dot{\rho} \sin(\lambda_\nu) & \frac{1}{\rho^2} \dot{\rho} \cos(\lambda_\nu) \\ 0 & 0 & 0 & 0 & +\frac{1}{\rho} \cos(\lambda_\nu) \dot{\nu} & +\frac{1}{\rho} \sin(\lambda_\nu) \dot{\nu} \end{bmatrix} \quad (37)$$

where  $\nu = \nu(t)$ ,  $\lambda_\nu = \omega + \nu(t)$ ,  $\rho = 1 + e \cos(\nu(t))$ ,  $\dot{\rho} = -e \sin(\nu) \dot{\nu}$ ,  $\eta = \sqrt{1 - e^2}$ ,  $n = \sqrt{\mu/a^3}$ , and  $\mu$  is the main gravitation parameter. The IC used in this paper are linked to the quasi-nonsingular ROE through the first order map

$$\mathbf{c}_k \approx \mathbf{M}_{HCW}(\boldsymbol{\alpha}) \begin{bmatrix} 1 & 0 & 0 & 0 & 0 & 0 \\ \frac{3}{2} nt & 1 & 0 & 0 & 0 & 0 \\ 0 & 0 & 1 & 0 & 0 & 0 \\ 0 & 0 & 0 & 1 & 0 & 0 \\ 0 & 0 & 0 & 0 & 1 & 0 \\ 0 & 0 & 0 & 0 & 0 & 1 \end{bmatrix} \begin{pmatrix} (a_k - a)/a \\ (\omega_k + M_k(t) - \omega - M(t)) + (\Omega_k - \Omega) \cos(i) \\ e_k \cos(\omega_k) - e \cos(\omega) \\ e_k \sin(\omega_k) - e \sin(\omega) \\ i_k - i \\ (\Omega_k - \Omega) \sin(i) \end{pmatrix} \quad (38)$$

where

$$\mathbf{M}_{HCW}(\boldsymbol{\alpha}) = \begin{bmatrix} \eta^2 & 0 & 0 & 0 & 0 & 0 \\ 0 & \frac{1}{\eta} & -(\eta^2 - \frac{1}{\eta}) \frac{\sin(\omega)}{e} & (\eta^2 - \frac{1}{\eta}) \frac{\cos(\omega)}{e} & 0 & (\eta^2 - \frac{1}{\eta}) \cot(i) \\ 0 & \frac{e \sin(\omega)}{\eta} & \cos^2(\omega) + \frac{\sin^2(\omega)}{\eta} & \cos(\omega) \sin(\omega) - \frac{\cos(\omega) \sin(\omega)}{\eta} & 0 & -\frac{e \sin(\omega) \cot(i)}{\eta} \\ 0 & -\frac{e \cos(\omega)}{\eta} & \cos(\omega) \sin(\omega) - \frac{\cos(\omega) \sin(\omega)}{\eta} & \sin(\omega)^2 + \frac{\cos(\omega)^2}{\eta} & 0 & \frac{e \cos(\omega) \cot(i)}{\eta} \\ 0 & 0 & 0 & 0 & \eta^2 & 0 \\ 0 & 0 & 0 & 0 & 0 & \eta^2 \end{bmatrix} \quad (39)$$

and, in the ROE,  $M(t)$  is the mean anomaly at instant  $t$ . The center matrix in Eq. 38 back-propagates the ROE to initial integration instant ( $t = 0$ ) through the integrable dynamics. For  $e \rightarrow 0$ ,  $\mathbf{M}_{HCW}$  becomes identity (the singularities cancel out), and the IC used in this paper reduce to the quasi-nonsingular ROE and to the HCW's IC [15]. The link between the IC used in this paper and the Yamanaka-Ankersen's IC is presented in [36].

## Acknowledgments

This work was supported by the William R. and Sara Hart Kimball Stanford Graduate Fellowship, and by the VISORS's mission NSF Award #1936663. The authors are thankful for their support.

## References

- [1] Jacklin, S. A., “Small-satellite mission failure rates,” Tech. Rep. TM-2018-220034, NASA, 2019. URL <https://ntrs.nasa.gov/api/citations/20190002705/downloads/20190002705.pdf>.
- [2] Dezfuli, H., Benjamin, A., Everett, C., Maggio, G., Stamatelatos, M., Youngblood, R., Guarro, S., Rutledge, P., Sherrard, J., Smith, C., and Williams, R., “NASA Risk Management Handbook. Version 1.0,” , 2011. URL <https://ntrs.nasa.gov/api/citations/20120000033/downloads/20120000033.pdf>.
- [3] Scharf, D. P., Açıkmese, B., Ploen, S. R., and Hadaegh, F. Y., “Three-dimensional re-active collision avoidance with multiple colliding spacecraft for deep-space and earth-orbiting formations,” *Fourth International Conference on Spacecraft Formation Flying Missions and Technologies*, 2011, pp. 1–4.
- [4] Starek, J. A., Schmerling, E., Maher, G. D., Barbee, B. W., and Pavone, M., “Fast, Safe, Propellant-Efficient Spacecraft Motion Planning Under Clohessy-Wiltshire-Hill Dynamics,” *Journal of Guidance, Control, and Dynamics*, Vol. 40, No. 2, 2017, pp. 418–438. <https://doi.org/10.2514/1.G001913>.
- [5] Hubert, S., and Swale, J., “Stationkeeping of a constellation of geostationary communications satellites,” *Astrodynamics Conference*, 1984, p. 2042. <https://doi.org/10.2514/6.1984-2042>.
- [6] D’Amico, S., and Montenbruck, O., “Proximity Operations of Formation-Flying Spacecraft Using an Eccentricity/Inclination Vector Separation,” *Journal of Guidance, Control, and Dynamics*, Vol. 29, No. 3, 2006, pp. 554–563. <https://doi.org/10.2514/1.15114>.
- [7] Breger, L., and How, J. P., “Safe Trajectories for Autonomous Rendezvous of Spacecraft,” *Journal of Guidance, Control, and Dynamics*, Vol. 31, No. 5, 2008, pp. 1478–1489. <https://doi.org/10.2514/1.29590>.
- [8] Barbee, B. W., Carpenter, J. R., Heatwole, S., Markley, F. L., Moreau, M., Naasz, B. J., and Van Eepoel, J., “A Guidance and Navigation Strategy for Rendezvous and Proximity Operations with a Noncooperative Spacecraft in Geosynchronous Orbit,” *Journal of the Aerospace Sciences*, Vol. 58, No. 3, 2011, pp. 389–408. <https://doi.org/10.1007/BF03321176>.
- [9] Woffinden, D. C., and Geller, D. K., “Navigating the Road to Autonomous Orbital Rendezvous,” *Journal of Spacecraft and Rockets*, Vol. 44, No. 4, 2007, pp. 898–909. <https://doi.org/10.2514/1.30734>.
- [10] D’Errico, M., *Distributed Space Missions for Earth System Monitoring*, Springer, New York, 2013.
- [11] Koenig, A. W., and D’Amico, S., “Robust and Safe N-Spacecraft Swarming in Perturbed Near-Circular Orbits,” *Journal of Guidance, Control, and Dynamics*, Vol. 41, No. 8, 2018, pp. 1643–1662. <https://doi.org/10.2514/1.G003249>.
- [12] Lakshmikantham, V., and Deo, S., *Method of Variation of Parameters for Dynamic Systems*, Series in Mathematical Analysis and Applications, Volume One, Gordon and Breach Science Publishers, Amsterdam, 1998.
- [13] Vallado, D. A., *Fundamentals of Astrodynamics and Applications*, Space Technology Library, 2013.
- [14] Clohessy, W. H., and Wiltshire, R. S., “Terminal Guidance System for Satellite Rendezvous,” *Journal of the Aerospace Sciences*, Vol. 27, No. 9, 1960, pp. 653–658. <https://doi.org/10.2514/8.8704>.
- [15] D’Amico, S., “Relative Orbital Elements as Integration Constants of Hills Equations,” *TN05-08, German Space Operations Centre (GSOC), Munich, Germany*, 2005.
- [16] Yamanaka, K., and Ankersen, F., “New State Transition Matrix for Relative Motion on an Arbitrary Elliptical Orbit,” *Journal of Guidance, Control, and Dynamics*, Vol. 25, No. 1, 2002, pp. 60–66. <https://doi.org/10.2514/2.4875>.
- [17] Sullivan, J., and D’Amico, S., “Nonlinear Kalman Filtering for Improved Angles-Only Navigation Using Relative Orbital Elements,” *Journal of Guidance, Control, and Dynamics*, 2017, pp. 1–18. <https://doi.org/10.2514/1.G002719>.
- [18] Gim, D.-W., and Alfriend, K. T., “State Transition Matrix of Relative Motion for the Perturbed Noncircular Reference Orbit,” *Journal of Guidance, Control, and Dynamics*, Vol. 26, No. 6, 2003, pp. 956–971. <https://doi.org/10.2514/2.6924>.
- [19] Koenig, A. W., Guffanti, T., and D’Amico, S., “New State Transition Matrices for Spacecraft Relative Motion in Perturbed Orbits,” *Journal of Guidance, Control, and Dynamics*, Vol. 40, No. 7, 2017, pp. 1749–1768. <https://doi.org/10.2514/1.G002409>.
- [20] Guffanti, T., D’Amico, S., and Lavagna, M., “Long-Term Analytical Propagation of Satellite Relative Motion in Perturbed Orbits,” *27th AAS/AIAA Space Flight Mechanics Meeting*, San Antonio, TX, 2017, pp. 1–31. URL [https://slab.stanford.edu/sites/g/files/sbiybj25201/files/media/file/sfm2017\\_guffantidamicolavagna.pdf](https://slab.stanford.edu/sites/g/files/sbiybj25201/files/media/file/sfm2017_guffantidamicolavagna.pdf).

- [21] Guffanti, T., and D’Amico, S., “Linear Models for Spacecraft Relative Motion Perturbed by Solar Radiation Pressure,” *Journal of Guidance, Control, and Dynamics*, Vol. 42, No. 9, 2019, pp. 1962–1981. <https://doi.org/10.2514/1.G002822>.
- [22] Chernick, M., “Optimal Impulsive Control of Spacecraft Relative Motion,” Ph.D. thesis, Stanford University, 2021. URL <https://purl.stanford.edu/vw016ts7713>.
- [23] Byrd, R. H., Gilbert, J. C., and Nocedal, J., “A Trust Region Method Based on Interior Point Techniques for Nonlinear Programming,” *Mathematical Programming*, Vol. 89, No. 1, 2000, pp. 149–185. <https://doi.org/10.1007/PL00011391>.
- [24] Liu, X., and Lu, P., “Solving Nonconvex Optimal Control Problems by Convex Optimization,” *Journal of Guidance, Control, and Dynamics*, Vol. 37, No. 3, 2014, pp. 750–765. <https://doi.org/10.2514/1.62110>.
- [25] Bonalli, R., Cauligi, A., Bylard, A., and Pavone, M., “GuSTO: Guaranteed sequential trajectory optimization via sequential convex programming,” *IEEE International Conference on Robotics and Automation (ICRA)*, Montreal, May, 2019, pp. 6741–6747. <https://doi.org/10.1109/ICRA.2019.8794205>.
- [26] Singh, S., “Robust Control, Planning, and Inference for Safe Robot Autonomy,” Ph.D. thesis, Stanford University, 2019. URL <https://purl.stanford.edu/pr731qc2534>.
- [27] Carpenter, J. R., and D’Souza, C. N., “Navigation filter best practices,” Tech. Rep. TP-2018-219822, NASA, 2018. URL <https://ntrs.nasa.gov/api/citations/20180003657/downloads/20180003657.pdf>.
- [28] Blackmore, L., Ono, M., and Williams, B. C., “Chance-Constrained Optimal Path Planning With Obstacles,” *IEEE Transactions on Robotics*, Vol. 27, No. 6, 2011, pp. 1080–1094. <https://doi.org/10.1109/TRO.2011.2161160>.
- [29] Borrelli, F., Bemporad, A., and Morari, M., *Predictive control for linear and hybrid systems*, Cambridge University Press, 2017.
- [30] Morgan, D., Chung, S.-J., and Hadaegh, F. Y., “Model Predictive Control of Swarms of Spacecraft Using Sequential Convex Programming,” *Journal of Guidance, Control, and Dynamics*, Vol. 37, No. 6, 2014, pp. 1725–1740. URL <https://doi.org/10.2514/1.G000218>.
- [31] Zhang, Y., and Jiang, J., “Bibliographical review on reconfigurable fault-tolerant control systems,” *Annual Reviews in Control*, Vol. 32, No. 2, 2008, pp. 229–252. <https://doi.org/10.1016/j.arcontrol.2008.03.008>.
- [32] Semsar-Kazerooni, E., and Khorasani, K., “Team Consensus for a Network of Unmanned Vehicles in Presence of Actuator Faults,” *IEEE Transactions on Control Systems Technology*, Vol. 18, No. 5, 2010, pp. 1155–1161. <https://doi.org/10.1109/TCST.2009.2032921>.
- [33] Guffanti, T., and D’Amico, S., “Integration Constants as State Variables for Optimal Path Planning,” *2018 European Control Conference (ECC)*, Cyprus, June 12–15, 2018, pp. 1–6. <https://doi.org/10.23919/ECC.2018.8550448>.
- [34] Guffanti, T., and D’Amico, S., “Multi-Agent Passive Safe Optimal Control using Integration Constants as State Variables,” *AIAA Scitech 2021 Forum*, 2021, p. 1101. <https://doi.org/10.2514/6.2021-1101>.
- [35] Guffanti, T., and D’Amico, S., “Robust Passively Safe Spacecraft Swarming via Closed-form and Optimization-based Control Approaches,” *American Control Conference*, Atlanta, Georgia, June 8–10, 2022, pp. 1–8.
- [36] Guffanti, T., “Optimal Passively-Safe Control of Multi-Agent Motion with Application to Distributed Space Systems,” Ph.D. thesis, Stanford University, 2022. URL <https://purl.stanford.edu/gh147jp5825>.
- [37] Koenig, A. W., D’Amico, S., and Lightsey, E. G., “Formation flying orbit and control concept for the VISORS mission,” *AIAA Scitech 2021 Forum*, 2021, p. 0423. <https://doi.org/10.2514/6.2021-0423>.
- [38] Boyd, S., and Vandenberghe, L., *Convex Optimization*, Cambridge University Press, 2004.
- [39] Domahidi, A., Chu, E., and Boyd, S., “ECOS: An SOCP solver for embedded systems,” *European Control Conference (ECC)*, 2013, pp. 3071–3076. <https://doi.org/10.23919/ECC.2013.6669541>.
- [40] Giraldo, V., “Precision Navigation of Miniaturized Distributed Space Systems using GNSS,” Ph.D. thesis, Stanford University, 2021. URL <https://purl.stanford.edu/dp334dn5706>.
- [41] Casotto, S., “The Equations of Relative Motion in the Orbital Reference Frame,” *Celestial Mechanics and Dynamical Astronomy*, Vol. 124, No. 3, 2016, pp. 215–234. <https://doi.org/10.1007/s10569-015-9660-1>.

- [42] Lightsey, E. G., Stevenson, T., and Sorgenfrei, M., “Development and Testing of a 3-D-Printed Cold Gas Thruster for an Interplanetary CubeSat,” *Proceedings of the IEEE*, Vol. 106, No. 3, 2018, p. 379–390. <https://doi.org/10.1109/JPROC.2018.2799898>.
- [43] Tapley, B. D., Bettadpur, S., Watkins, M., and Reigber, C., “The Gravity Recovery and Climate Experiment: Mission Overview and Early Results,” *Geophysical Research Letters*, Vol. 31, No. 9, 2004, pp. 1–4. <https://doi.org/10.1029/2004GL019779>.
- [44] Picone, J. M., Hedin, A. E., Drob, D. P., and Aikin, A. C., “NRLMSISE-00 empirical model of the atmosphere: Statistical comparisons and scientific issues,” *Journal of Geophysical Research: Space Physics*, Vol. 107, No. A12, 2002, pp. SIA–15. <https://doi.org/10.1029/2002JA009430>.
- [45] Gaias, G., and D’Amico, S., “Impulsive Maneuvers for Formation Reconfiguration Using Relative Orbital Elements,” *Journal of Guidance, Control, and Dynamics*, Vol. 38, No. 6, 2015, pp. 1036–1049. <https://doi.org/10.2514/1.G000189>.